2019

A numerical model of the high-temperature supercritical tube flow produced by the NTREES nuclear thermal propulsion test facility

Connor T. Pierce

Recommended Citation

Pierce, Connor T., "A numerical model of the high-temperature supercritical tube flow produced by the NTREES nuclear thermal propulsion test facility" (2019). *Theses*. 640.
https://louis.uah.edu/uah-theses/640

A NUMERICAL MODEL OF THE HIGH-TEMPERATURE SUPERCRITICAL TUBE FLOW PRODUCED BY THE NTREES NUCLEAR THERMAL PROPULSION TEST FACILITY

by

CONNOR T. PIERCE

A THESIS

Submitted in partial fulfillment of the requirements
for the degree of Master of Science
in
The Department of Mechanical and Aerospace Engineering
to
The School of Graduate Studies
of
The University of Alabama in Huntsville

HUNTSVILLE, ALABAMA

2019

In presenting this thesis in partial fulfillment of the requirements for a master's degree from The University of Alabama in Huntsville, I agree that the Library of this University shall make it freely available for inspection. I further agree that permission for extensive copying for scholarly purposes may be granted by my advisor or, in his absence, by the Chair of the Department or the Dean of the School of Graduate Studies. It is also understood that due recognition shall be given to me and to The University of Alabama in Huntsville in any scholarly use which may be made of any material in this thesis.

2/22/19

(student signature) (date)

THESIS APPROVAL FORM

Submitted by Connor Pierce in partial fulfillment of the requirements for the degree of Master of Science in Engineering with an option in Mechanical Engineering and accepted on behalf of the Faculty of the School of Graduate Studies by the thesis committee.

We, the undersigned members of the Graduate Faculty of The University of Alabama in Huntsville, certify that we have advised and/or supervised the candidate on the work described in this thesis. We further certify that we have reviewed the thesis manuscript and approve it in partial fulfillment of the requirements for the degree of Master of Science in Engineering with an option in Mechanical Engineering.

________________________________ Committee Chair
Dr. D. Keith Hollingsworth (Date)

William Emrich
____
Dr. William Emrich

____
Dr. Kader Frendi

________________________________ Department Chair
Dr. D. Keith Hollingsworth

________________________________ College Dean
Dr. Shankar Mahalingam

________________________________ Graduate Dean
Dr. David Berkowitz

ABSTRACT

The School of Graduate Studies
The University of Alabama in Huntsville

Degree Master of Science in Engineering College/Dept. Engineering/Mechanical and Aerospace Engineering

Name of Candidate Connor T. Pierce

Title A Numerical Model of the High-Temperature Supercritical Tube Flow Produced by the NTREES Nuclear Thermal Propulsion Test Facility

A numerical investigation was performed of heat transfer in a supercritical hydrogen tube flow at wall temperatures up to 2500 K. The study was motivated by the propellant flow exhibited in the Nuclear Thermal Rocket Element Environment Simulator (NTREES) developed at NASA Marshall Space Center. A single coolant channel 40.6 cm in length and 0.381 cm in diameter was simulated in ANSYS-Fluent. Both constant and variable material properties were investigated for supercritical hydrogen at approximately 2.5 times the critical pressure. Two wall heat flux boundary conditions were examined: uniform flux and a streamwise cosine flux profile which is a typical profile used to model nuclear thermal rocket power density.

Three mass fluxes from 185 to 425 kg/m^2s produced Reynolds numbers up to 80,000 for the variable property runs. The ANSYS Fluent simulations used a Reynolds-averaged Navier-Stokes solver with a k-ω SST 2-equation turbulence model. The simulations were validated for uniform-property flow by comparison to accepted correlations for the streamwise evolution of Nusselt number in a developing turbulent flow.

The study using the uniform-flux boundary condition concluded that, at the heat flux levels investigated, the Nusselt number in the developing portion of the channel is lower than given by accepted correlations for fully developed flow and lower than the fully developed values for the variable-property flow. This behavior is accompanied by a significant increase in wall temperature above expected values in the developing region. These differences were present at far smaller levels for the cosine-flux boundary condition due to the lower heat flux levels generated in the developing region. Several Nusselt number correlations from the literature for heat transfer into supercritical hydrogen were compared to the model results.

Abstract Approval: Committee Chair
Department Chair
Graduate Dean

DEDICATION

To my Mother.

ACKNOWLEDGEMENTS

First and foremost, I would like to thank my advisor, Dr. Keith Hollingsworth for the many hours spent guiding me through the investigation process of this research study. He has the unique ability to link high level heat transfer physical phenomena with daily life, which proved to be an invaluable asset during my time at UAH. I owe thanks to Dr. Bill Emrich for the introduction to the field that is nuclear fission propulsion systems in both the classroom and this research endeavor, as Dr. Emrich is the project manager for the NTREES facility at MSFC. A thank you needs to be given to both Dr. Kader Frendi and Dr. Sarma Rani for their exceptionally valuable classroom lectures and outside discussions on turbulent flows and modeling methodology. Mr. Euan Holton needs thanks, for without him maintaining the workstations on which the simulations ran, this research could not be possible. Lastly, a thanks to Dr. John Willard for his many hours of overseeing and critiquing both my coding and numerical simulations to insure best practices were conducted.

TABLE OF CONTENTS

LIST OF FIGURES

LIST OF TABLES

NOMENCLATURE

Symbol	Description	Units
	Lowercase Roman	
a, b, c	Heat flux function terms	-
C_f	Skin friction coefficient	-
f	Friction factor	-
g_c	Conversion factor	$\frac{kg\, m}{N s^2}$
h_c	Heat transfer coefficient	$\frac{W}{m^2 K}$
k	Thermal Conductivity, Turbulent kinetic energy	$\frac{W}{mK}, \frac{J}{kg}$
$k^+ \equiv \frac{k}{u_\tau^2}$	Dimensionless turbulent kinetic energy	-
$\dot{m}$	Mass flow rate	$\frac{kg}{s}$
$\dot{m}''$	Mass flux rate	$\frac{kg}{m^2 s}$
q''	Heat flux	$\frac{W}{m^2}$
q^+	Dimensionless heat flux	-
r	Radius (local position)	m

$u_\tau \equiv \sqrt{\frac{\tau_w}{\rho}}$	Friction velocity	$\frac{m}{s}$
$\vec{v}$	Velocity vector	$\frac{m}{s}$
y	Normal distance from tube wall (Traverse coordinate)	m
$y^+ \equiv \frac{y u_\tau}{\nu}$	Dimensionless normal distance from tube wall	-

Uppercase Roman

A	Area	m^2
C_p	Constant pressure specific heat	$\frac{J}{kgK}$
D	Diameter	m
D_ω	Flow Cross-Diffusion Term	-
E	Energy	J
$\vec{F}$	Force vector	N
G_k, G_ω	Generation Terms	-
I_{sp}	Specific Impulse	$s, \frac{m}{s}$

L	Length of tube	m
M	Molecular weight	u
Nu	Nusselt number	-
P	Pressure, Power Flux	$Pa, \frac{W}{m^2}$
$Pe \equiv RePr$	Peclet number	-
$Pr \equiv \frac{\nu}{\alpha}$	Prandtl number	-
R	Radial dimension, Hydrogen gas constant	m, $\frac{J}{kgK}$
$Re_D \equiv \frac{\dot{m}'' D}{\mu}$	Reynolds number (Mass flux referenced)	-
S_h, S_k, S_ω	Scalar Source Terms	-
$St \equiv \frac{h_c}{\rho C_p U_{ref}}$	Stanton number	-
T	Temperature	K
$T^+ \equiv \frac{\theta}{St}$	Dimensionless Temperature	-
U	Velocity parallel to the wall	$\frac{m}{s}$

$U^+ \equiv \frac{U}{u_\tau}$	Dimensionless velocity	-
Y_k, Y_ω	Dissipation Terms	-
Z	Streamwise axial position	m
Z/D	Dimensionless streamwise position	-
$Z^* \equiv Z/L$	Dimensionless streamwise unity position	-

Lowercase Greek

α	Core buckling term	$\frac{1}{cm}$
$\gamma \equiv \frac{C_p}{C_v}$	Ratio of specific heats	-
ε	Relative pipe roughness coefficient, Rate of dissipation of turbulent kinetic energy	- , $\frac{J}{kgs}$
κ	Von Karman Constant	-
μ	Dynamic viscosity	$Pa * s$
ν	Kinematic viscosity	$\frac{m^2}{s}$
ρ	Density	$\frac{kg}{m^3}$

$\tau_w \equiv \mu\left(\frac{\partial u}{\partial y}\right)\vert_{y=0}$	Wall shear force	$\frac{kg}{s^2 m}$
$\bar{\bar{\tau}}$	Stress tensor	-
φ	Parameter of choice in Mass Avg. Eq.	-
$\omega \equiv \frac{\varepsilon}{k}$	Specific rate of dissipation of turbulent kinetic energy (Turbulence frequency)	$\frac{1}{s}$

Uppercase Greek

Γ	Effective molecular diffusivity	$\frac{m^2}{s}$
$\theta \equiv \frac{T-T_w}{T_b-T_w}$	Dimensionless temperature parameter	-
$\boldsymbol{\Omega}$	$= \frac{Energy\ Addition\ (L)}{Mass\ Flow} = \frac{4q''\left(\frac{Z}{D}\right)}{\dot{m}''}$	$\frac{kJ}{kg}$

Subscript

b	Bulk referenced	-
c	Combustion chamber referenced (Reactor)	-
D	Diameter length scale referenced	-
eff	Effective referenced	-

i	Initial or entrance referenced	-
k	Turbulent kinetic energy referenced	-
t	Turbulence referenced	-
w	Wall referenced	-
ω	Specific rate of dissipation of turbulent kinetic energy referenced	-

CHAPTER 1

Introduction

Nuclear Thermal Rocket Operation and Experimental Facility Overview

There has always been substantial interest around alternative space propulsion methods and technology. As mankind progresses farther into outer space, our means to propel us there continues to be a major limiting factor. The push to replace current chemical propulsion methods requires exploring various other propulsion systems with the hope of achieving significant gains in the propulsion system's specific impulse I_{sp} (for formal definition, see Chapter 3). While technologies like electric propulsion and solar sails produce unmatched specific impulse, they significantly lack thrust to maneuver heavy payloads. This is where nuclear propulsion and nuclear thermal rockets (NTR) come into play.

As seen in **Figure 1.1**, nuclear thermal rockets bridge the gap between the high thrust, low I_{sp} achieving chemical propulsion methods and the low thrust, high I_{sp} methods mentioned. With further development, NTRs have the potential to be mankind's ticket to distant parts of outer space or even just a cheap and efficient means to propel vessels within our own solar system.

NTRs utilize the same working principles as chemical propulsion systems. That is, they use an energy source to heat a propellant. This gives the propellant thermal energy to trade for a change in velocity as it is exhausted through a converging-diverging nozzle to produce thrust **[1]**. Unlike chemical propulsion systems which are energy limited, NTRs are power density limited **[2]**. This means the energy potential of the NTR systems are limited by melting temperatures of the radioactive fuel rod materials utilized. Chemical propulsion has essentially reached the height of its potential, but as research into high temperature materials evolve, the capabilities of NTRs will begin to shine and possibly surpass current conventional methods for space travel.

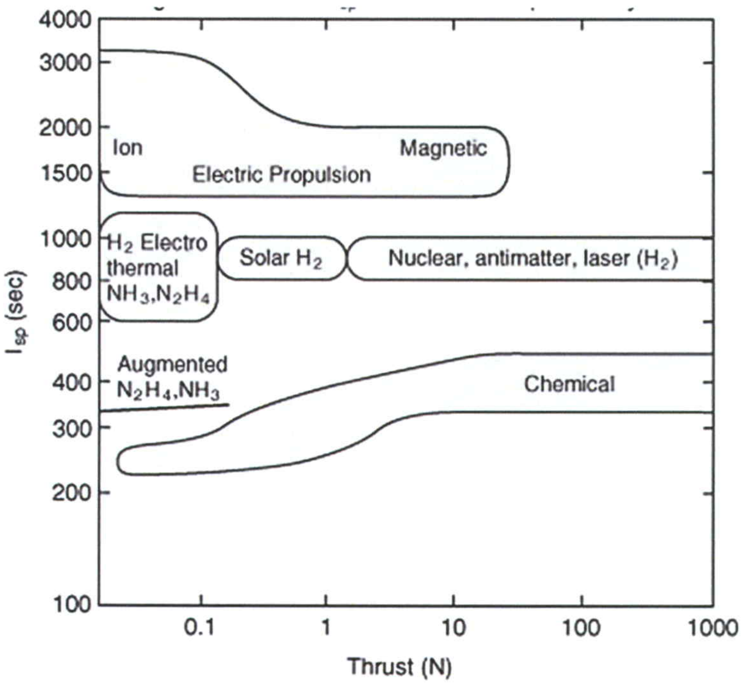

Figure 1.1: Thrust vs. I_{sp} for Various Space Propulsion Systems ***[3]***

NTR Operation Overview and Significance

As the current investigation is ultimately about NTR development, first it is important to discuss the general concepts surrounding how NTR's operate. It is, at its essence, a rather straight forward concept. Using **Figure 1.2** of a "Hot Bleed" cycle for reference, the Liquid Hydrogen (LH_2) is stored in propellant tanks. The LH_2 is then fed at operating pressure through the cold/pump side of a turbopump to be distributed to various components of the propulsion system such as the nozzle and reactor chamber walls for regenerative cooling. At this point, the LH_2 becomes gaseous due to the enthalpy gain. The propellant then enters the nuclear reactor core to be heated by the fissionable material radiating inside the reactor's fuel elements, with a small portion entering the hot/turbine side of a turbo pump as its power source to continue pumping new LH_2 into the propulsion system before being exhausted. The bulk propellant that enters the reactor core is exposed to extreme levels of heat flux given off by the reactor itself. The propellant is heated to temperatures upwards of 2500 K **[4]**. At the exit of the reactor, a small portion of hot propellant is then fed to the hot/turbine side of the turbopump to be mixed with the other, cooler bleed source propellant to aid in powering the turbopump, hence the "Hot Bleed" cycle. Finally, most of the propellant that was not used for powering the turbopump, yet entered the reactor, is now exhausted through a converging-diverging nozzle to exchange the huge quantities of thermal energy gained for kinetic energy (i.e. a drastic increase in velocity). The momentum of the exiting jet produces thrust.

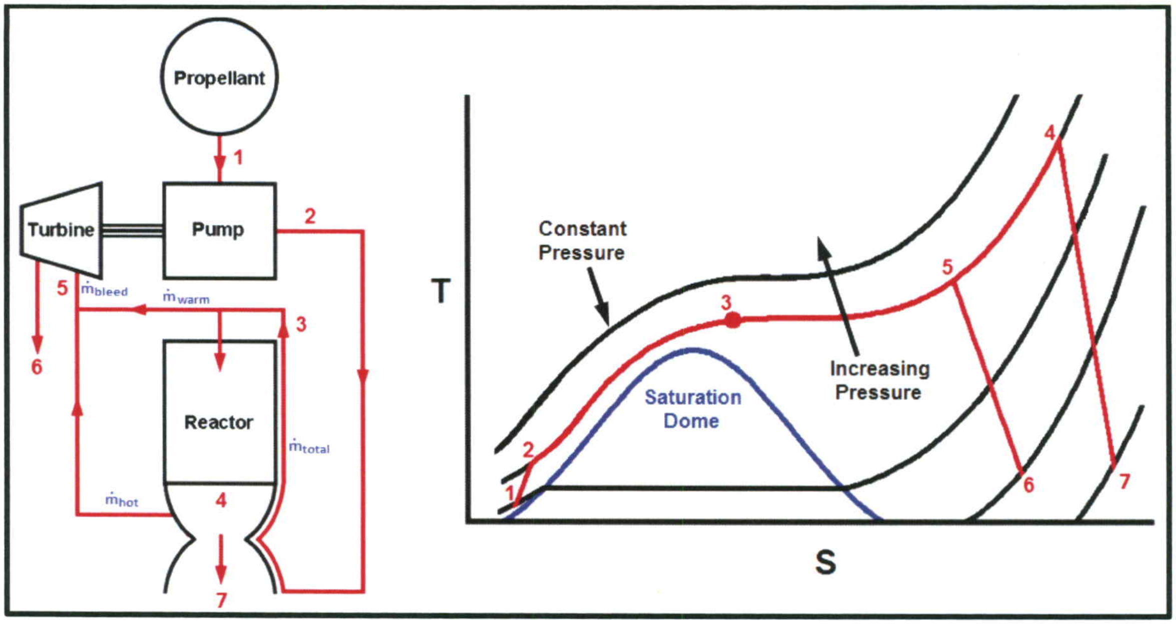

Figure 1.2: NTR "Hot Bleed Cycle" Flow Diagram ***[2]***

The principle of superheating a gas to be expelled from a nozzle for the exchange of thermal to kinetic energy is the same for both chemical and nuclear rocket propulsion. In short, the primary difference is a chemical system uses a propellant and oxidizer burning, where a nuclear system uses the radiating heat given off by a fissioning material **[4]**.

It should be noted recent design variants for long-duration, manned missions such as a mission to Mars have mostly shifted to that of an "Expander" cycle for its much more efficient use of H2 propellant and cooler turbine inlet temps keeping stress levels more manageable **[5], [6], [7]**. A schematic of an NTR expander cycle can be seen in **Figure 1.3**.

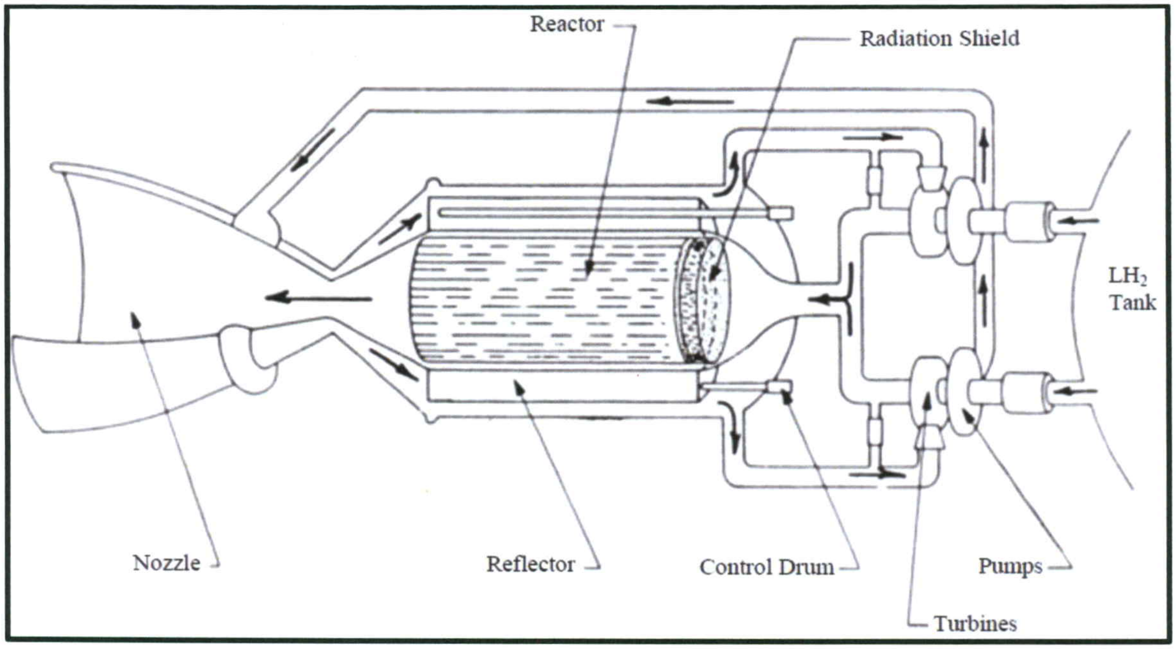

Figure 1.3: NTR "Expander Cycle" Flow Diagram ***[5]***

The reactor of a NTR is composed of fuel elements containing fissionable material (typically uranium 235, U-235). The enriched fissionable material acts as the thermal energy source typically contained in a cermet material matrix capable of withstanding long durations at high temperatures and moderate pressures. A graphite matrix was used during the NERVA/Rover program. However, due to fuel elements/cladding fractures causing high mass loss rates, and difficulties with graphite interacting chemically with hot H_2 to produce gases such as methane and acetylene more recent research has posed a matrix of tungsten to hold fissionable UO_2 **[8]**. The tungsten was chosen as it is far less affected by H_2 corrosion, chemically stable and has a higher creep strength.

The fuel elements are extruded into a long rod geometry with cooling channels for the H_2 propellant to flow through. Then, elements are oriented into a bundle housed within a pressure vessel lined circumferentially with control drums acting as the throttling mechanism for a NTR reactor's power output (See **Figure 1.4**).

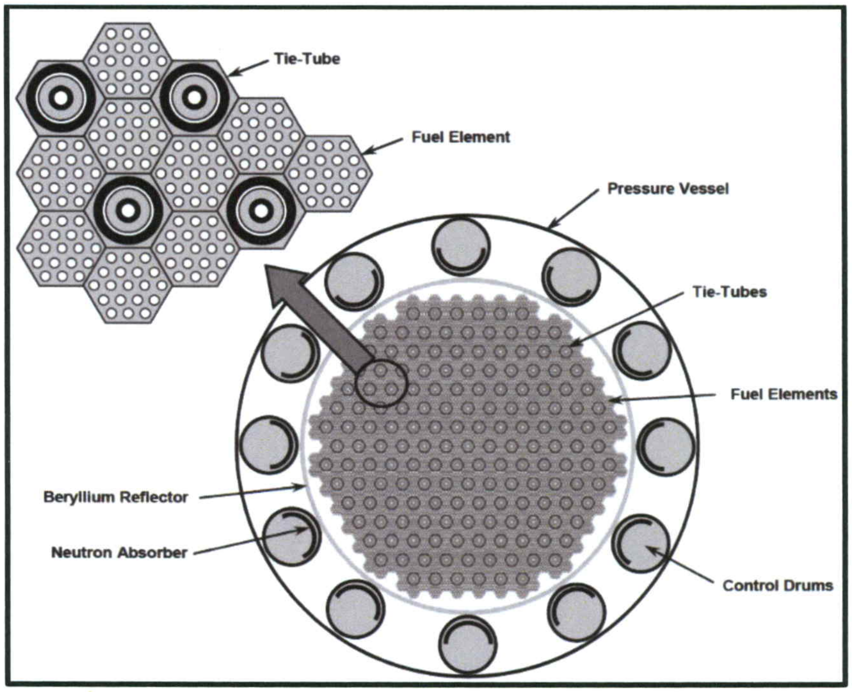

Figure 1.4: NTR Reactor Cross Section ***[7]***

NTREES-Nuclear Thermal Rocket Element Environmental Simulator

Located at NASA's Marshall Space Flight Center in Huntsville, Alabama resides the Nuclear Thermal Rocket Element Environmental Simulator (NTREES). NTREES is an impressive technological facility developed and optimized by Dr. William Emrich. As its name suggests, NTREES was designed to further testing and research for the NTR fuel rod materials. The facility follows the work done by programs such as the Nuclear Engine for Rocket Vehicle Application (NERVA, a joint effort between the AEC/NASA, see more details in Chapter 2) or RD-0410 (Russian NTR engine).

In its current state, the facility (see **Figure 1.5**) utilizes a water-cooled pressure vessel capable of operating pressures up to 6.9 MPa. The facility is designed to handle maximum fuel rod test element dimensions of 2.50 m long by 0.30 m in diameter. The system can run at temperatures upwards of 3500 K and has two different gas feed systems. The first gas feed is hydrogen which serves as the NTR propellant and will enter cooling channels extruded into the fuel rod element. For more on the rod geometry, see Chapter 3 **[9], [10]**. The mass flow rate range for the hydrogen is 0-250 gm/s. The second gas fed into NTREES is nitrogen as a mass flow rate range of 0-700 gm/s. Nitrogen mixes with the hot H_2 exiting the test fuel element producing a safe, inert mixture prior to exhausting to the outside environment. To simulate the heat generated by the fissionable material in an actual NTR fuel element, NTREES is equipped with a water cooled, 1. 2 MW induction heating coil which surrounds the test element.

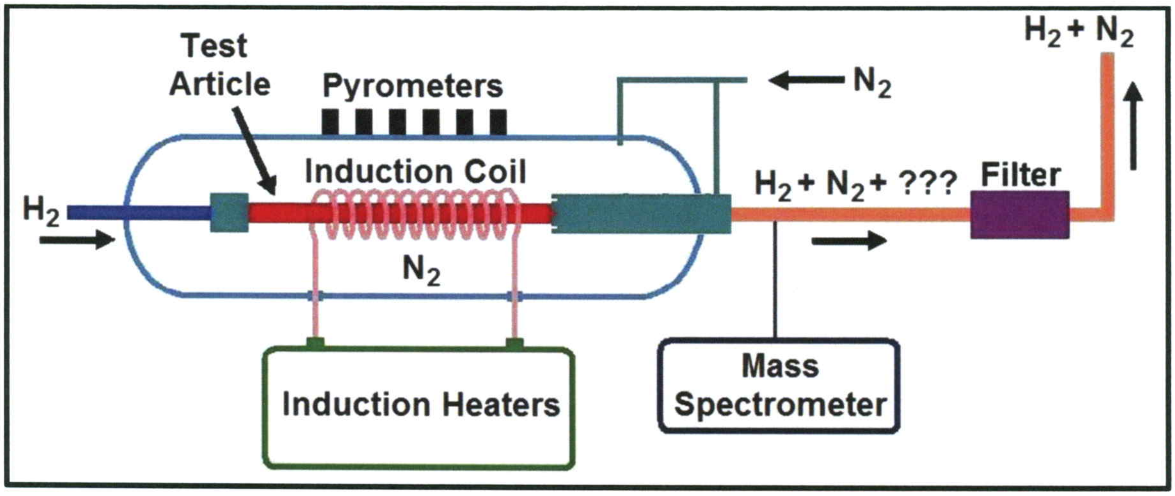

Figure 1.5: NTREES Operational Layout ***[10]***

As stated previously, NTREES was created to test samples of NTR fuel rod. The samples vary in overall dimensions, but for the most part maintain the same general geometry. That being an extruded rod with a distribution of extruded circular channels in the streamwise hydrogen flow direction (see **Figure 1.4**). The channels are typically cladded with a zirconium carbide (ZrC) coating to protect the inner fuel rod material from being degraded by the supercritical hydrogen flowing through the channels **[7]**. The development of these fuel rods is critical to the overall success of NTR as a viable means of propulsion. The rods currently experience temperatures in excess of 2500 K. With such a rapid increase in temperature, it is important to consider the coefficient of thermal expansion for both the fuel rod material itself and the cladding utilized on the inner channel walls. When these coefficients differ significantly, fracturing can occur in area which the channel wall temperature gradients are at a maximum in the streamwise flow direction. The analysis of these failure modes leads to design improvements to mitigate cladding fracturing. It is crucial to mimic environmental conditions an in-flight NTR will experience as best as feasibly possible.

A fuel rod operating within an NTR would experience quite a uniform heat flux profile across its cross section due to the UO_2 dispersed within the rod's matrix. One of the current limitations of NTREES is its ability to only test a singular fuel rod at a time that is inductively heated. In an actual NTR, as mentioned previously, the rods reside in a bundle such that the outer walls of each rod are in contact. What does this mean for NTREES? First, the inductive heating coil in NTREES creates a non-linear bias of heat flux towards the outer radius of test elements. Second, the testing of single fuel rods means the outer surface area of the rod is exposed to the pressure vessel environment. That is, it expels heat energy via convection and radiation (especially radiation towards the hot exit end of the rod). This inconsistency with conditions seen by fuel rods during actual NTR firings has the potential to induce additional failure modes that may only exist within the testing facility. That premise laid the foundation and framework for the current study.

Motivation for the Present Study

The current interest in modeling the temperature and strain field distribution within the fuel rod test element of the NTREES facility is the motivation for the present study. An important element of such a model would be the heat transfer coefficients generated on the propellant tube walls along the length of the fuel rod. The flow in question is a turbulent flow of supercritical H_2 where the development length of the tube flow occupies a large fraction of the fuel rod length. The NTREES facility produces very high heat flux (3.5 MW/m^2 in the present model) and this drives large radial and axial variations in the thermophysical properties of the H_2 while flow is developing in the tube. This situation is quite far from canonical flows described in heat transfer texts, but correlations have been developed for particular cases of supercritical heated gas flows. Some of these correlations were developed by the NTR research community. These correlations and the studies that produced them will be reviewed in Chapter 2.

The present study seeks to build a computational model of a single cooling channel from an NTREES test element using a variable-property Reynolds-Averaged Navier-Stokes (RANS) approach. The model was executed in ANSYS-Fluent and required the creation of thermodynamic and thermophysical property tables within Fluent via the User Defined Function (UDF) facility. The single-tube geometry was built within a cartesian coordinate system in such a way that the model can be scaled up to include multiple cooling channels separated by a solid rod domain. The model was executed for two thermal boundary conditions: uniform wall flux and a cosine-flux axial distribution that is a common model in the NTR community. The results of the study serve two primary purposes: (1) axial values of heat transfer coefficient (Nusselt number) are produced that can be used directly in NTREES fuel rod models, and (2) the Nusselt number results can be compared to the predictions of correlations from the literature for flows of this type.

Mesh selection was validated by a run with constant fluid properties and a uniform wall flux. The results were compared to the classical solution for constant-heat-flux tube flow. The mesh was refined, and each resulting model converged toward the classical solution for Nusselt number. The simulation was then run with variable material properties and a constant and high wall heat flux representing that produced by the NTREES facility. Streamwise evolution of the wall temperature and Nusselt number were examined along with radial profiles of streamwise velocity and fluid temperature. Following this, a cosine axial heat flux profile was applied with variable material properties to simulate the flux conditions in an NTR. Finally, Nusselt number plots were compared against several known correlations discussed in Chapter 2.

CHAPTER 2

Literature Overview

The future of nuclear thermal rockets has been a point of heavy debate and interest for more than 60 years. These systems exhibit a huge potential as a long-distance propulsion system due to very high specific impulse while maintaining a substantial amount of thrust to move large payloads effectively. As NTR's are a viable option for future space missions of long durations with further development, studies on said development have been consistently produced ever since the original NERVA program.

The work reviewed in this chapter will be split into the following subsections: experimental studies and data from full NTR engine tests (US research only), Nusselt number correlations for high temperature supercritical fluids in cooling channels, a review of studies of developing internal flows, and computational fluid dynamics (CFD) studies of propellant flows through the fuel element cooling channels.

Experimental Studies and Data from Full NTR Engine Tests

Due to funding, health and political reasons, a full-scale NTR engine test fire has not occurred since the NERVA/Rover days of research (1955-1972) **[11]**. The Nuclear Engine for Rocket Vehicle Applications (NERVA) program set out to establish a "Proof of Concept" NTR model showing the strengths and finding the weaknesses of nuclear propulsion methods. The full-scale reactor/engine tests were conducted by Los Alamos National Laboratory out of the Nuclear Rocket Development Station (NRDS) situated in Jackass Flats, Nevada. Although the project involved multiple different organizations and contractors, the NERVA project was split into two primary organizations responsible for major development and funding. NASA funded development of various flight subsystems, engine test stands, support facilities and, in general, components of NERVA that are non-nuclear. The Atomic Energy Commission (AEC) funded nuclear component development such as reactors and fuel element research. As nuclear elements were to be in close proximity with other subsystems and flight hardware, it was critical that the development of all major subsystems be done as a joint effort. This was to insure the operation of subsystems exposed to radiation would remain reliable and acceptable for spaceflight **[12]**.

In late 1955, the concept for a "solid-core, hydrogen-cooled reactor" was entering its design process and by mid-1959, a test of the first reactor named KIWI-A was successfully conducted for a total duration of 5 minutes at 70 MW of power **[13]**. As the NERVA project progressed, its team learned and continued to develop the NTR engine designs reducing failure modes, increased reliability during prolonged engine up time during both steady and transient operation, increased re-start reliability without the means of external power, increased power output and found the optimum balance between safety, efficiency I_{sp} and thrust. By the end of the NERVA program, 20 reactor tests and 2 full engine tests were conducted **[12]**. The reactor technology was refined, mass loss due to corrosion drastically reduced and average reactor temperatures increased. The project's initial goal of developing a "Proof of Concept" NTR was met and exceeded.

Nusselt Number Correlations

Dittus-Boelter

The Nusselt number is a dimensionless heat transfer coefficient,

$$Nu \equiv \frac{h_c D}{k_{fluid}} \qquad \textbf{Eq. (2.1)}$$

The Nusselt number can be expressed as the product of the Stanton, Reynolds and Prandtl numbers,

$$Nu \equiv St Re_D Pr \qquad \textbf{Eq. (2.2)}$$

where,

$$St \equiv \frac{h_c}{\rho C_p U_{ref}} \qquad \textbf{Eq. (2.3)}$$

$$Re_D \equiv \frac{\rho U D}{\mu} \equiv \frac{4\dot{m}}{\pi D \mu} \qquad \textbf{Eq. (2.4)}$$

$$Pr \equiv \frac{\nu}{\alpha} \equiv \frac{\mu C_p}{k} \qquad \textbf{Eq. (2.5)}$$

The oldest *Nu* correlation for fully developed turbulent pipe flow at moderate Prandtl number (*Pr*) and uniform material properties is the Dittus-Boelter correlation (1930), **Equation 2.6 [14]**. Dittus-Boelter applies reasonably to both uniform wall temperature and uniform wall heat flux boundary conditions as *Nu* differs little between these boundary conditions for a turbulent duct flow.

$$Nu_b = 0.023{Re_b}^{0.8}{Pr_b}^{0.4} \qquad \textbf{Eq. (2.6)}$$

The correlation follows, and perhaps established, the product-power-law form of heat transfer correlations and produces reasonably accurate *Nu* predictions with minimal information about the flow itself which is excellent for engineering or experimental solutions. Dittus-Boelter shows best results for fully developed (momentum and thermal) flows for $Re_D \geq 1.0 \times 10^4$, and $0.6 \leq Pr \leq 1.0 \times 10^4$.

Gnielinksi

Over the decades since the introduction of Dittus-Boelter, a number of correlations have been proposed which attempt to address a broader range of flow parameters, wall surface conditions, and property variations. One such correlation by Gnielinski, unlike Dittus-Boelter, incorporates a non-constant pipe friction factor term based off inlet/exit pressure loss (head loss) allowing *Nu* to be linked to head loss in noncanonical flow such as flows with a significant level of pipe wall roughness. The Gnielinski correlation **Equation 2.7** is best used for fully developed (thermal and momentum) pipe flows ranging from $3.0 \times 10^3 \leq Re_D \leq 5.0 \times 10^6$, $0.5 \leq Pr \leq 2.0 \times 10^3$ **[15]**. The friction factor term in said correlation (Darcy-Weisbach friction factor) is classically handled by a Moody chart plotted via the Darcy-Weisbach equation over various Re_D or the Colebrook-White equation. For this study however, the friction factor was obtained from the Zigrang-Sylvester **Equation 2.8** as it was shown to yield the most accurate results in a comparison study against other equations (including Colebrook-White) conducted by Genic, Arandjelovic (et. al.) **[16]**.

For the Zigrang-Sylvester equation the applicable flow ranges are $4.0 \times 10^3 \leq Re_D \leq 1.0 \times 10^8$ and $4.0 \times 10^{-6} \leq \varepsilon \leq 5.0 \times 10^{-2}$. Where ε is the relative pipe roughness coefficient.

$$Nu = \frac{(Re_D - 1000)(\frac{f}{2})\mathrm{Pr}}{1.0 + 12.7\left[\left(\frac{f}{2}\right)\left(Pr^{\frac{2}{3}} - 1.0\right)\right]^{1/2}} \quad \textbf{Eq. (2.7)}$$

$$f = \left\{-2\log_{10}\left[\frac{\varepsilon}{3.7} - \frac{5.02}{Re}\log_{10}\left(\varepsilon - \frac{5.02}{Re}log\left(\frac{\varepsilon}{3.7} + \frac{13}{Re}\right)\right)\right]\right\}^{-2} \quad \textbf{Eq. (2.8)}$$

Correlations Including Variable Properties

Sieder-Tate

Both Dittus-Boelter and Gnielinski are well-established for relatively constant property flows; however, in an NTR flow where the wall and bulk temperatures, as well as the streamwise temperatures vary greatly, one needs to start looking into correlations that consider large temperature and material property gradients. The Sieder-Tate correlation, **Equation 2.9**, is one approach **[17]**. The Sieder-Tate equation includes variations in dynamic viscosity with large differences in temperature between the local wall and bulk fluid values. The correlation is quite old (1936), making it one of the first equations of its kind to take variable properties effects into consideration. Like Dittus-Boelter, it is still regularly used and traceable in many variable properties works and texts today.

$$Nu = 0.027Re^{\frac{4}{5}}Pr^{\frac{1}{3}}\left(\frac{\mu_b}{\mu_w}\right)^{0.14}$$ **Eq. (2.9)**

Thomas and Taylor

The Thomas correlation **[18]** seen in **Equation 2.10** has a power-law construction similar to Dittus-Boelter apart from two differences. First, Thomas incorporates a temperature ratio term accounting for radial property changes and a term that is a function of streamwise position $\left(\frac{Z}{D}\right)$ to extend the correlation upstream into the development region. Thomas developed this correlation over the following flow ranges: $1.0 \times 10^4 \leq Re_D \leq 1.0 \times 10^5$, $0.6 \leq Pr \leq 1$, $0 \leq \left(\frac{Z}{D}\right) \leq 24$, $1 \leq \left(\frac{T_w}{T_b}\right) \leq 10$, and $50 \leq T_w$ (K) ≤ 2222.

$$Nu_b = 0.025{Re_b}^{0.8}{Pr_b}^{0.4}\left(\frac{T_w}{T_b}\right)^{-0.55}\left(1 + 0.3\left(\frac{Z}{D}\right)^{-0.7}\right)$$ **Eq. (2.10)**

It should be noted that Thomas realized the correlation had room for optimization as experimental work in high-temperature hydrogen thermophysical properties progressed. He mentions the correlation should not be used for flows at cryogenic temperatures. The Thomas document **[18]** also discusses many previous works in hot turbulent single-phase hydrogen tube flows and their various limitations.

Although Taylor developed many correlations for supercritical turbulent fluid flows inside heated pipes, the Taylor correlation **[19]** given as **Equation 2.11** has been highly cited for use with turbulent hydrogen channel flows with large wall to bulk temperature ratios. This correlation has a form unlike those reviewed to this point. Taylor places the streamwise dependence into a term that appears as a power on the temperature ratio, $\left(\frac{T_w}{T_b}\right)$. The Taylor correlation was built to reflect experimental results available at the time for a large range of flow conditions ($7.5 \times 10^3 \leq Re_D \leq 13.8 \times 10^6$, $0.6 \leq Pr \leq 10$, $2 \leq \left(\frac{Z}{D}\right) \leq 252$, $1.1 \leq \left(\frac{T_w}{T_b}\right) \leq 27.6$, and $29.5 \leq T_w$ (K) ≤ 3110). These conditions reflect NTR flows and regenerative cooling flows commonly seen in aerospace. It has been used with hydrogen, helium and nitrogen **[19], [20], [21]**. For a complete range of conditions considered by Taylor see **[19, Table 1]**.

$$Nu_b = 0.023 Re_b{}^{0.8} Pr_b{}^{0.4} \left(\frac{T_w}{T_b}\right)^{-\left(0.57-1.59/\frac{Z}{D}\right)} \qquad \textbf{Eq. (2.11)}$$

Note that the sign on the temperature ratio $\left(\frac{T_w}{T_b}\right)$ changes very near the tube entrance at $\left(\frac{Z}{D}\right) = 2.79$. Downstream of that location the power on $\left(\frac{T_w}{T_b}\right)$ is a slowly decreasing negative fraction (more strongly negative with streamwise distance). At $\left(\frac{Z}{D}\right) = 100$ downstream, the power is -0.554.

Taylor's correlation equation has been used to correlate the behavior of cryogenic hydrogen such as in Youn and Mills' research discussed later in Chapter 2 **[22]**. Also, NERVA and PHOEBUS-2 regenerative cooling rocket nozzle heat transfer coefficients were shown to be best predicted via the Taylor correlation (or variants of) for both straight flow and curved flow channel geometries **[23]**. Finally, work by Slaby and Mattson on high-temperature hydrogen flowing through passages in electrically heated tungsten rod elements supports the Taylor correlation for heat transfer predictions in an NTR like environment **[24]**.

Correlations Including Variable Properties and Variable Wall Heat Flux

McEligot (et. al.) and Pfriem

As explained in Donne and Tartaglia's review of Nusselt number correlations for supercritical hydrogen and helium **[25]**, most correlations incorporate a single streamwise locating term (if any at all). In order to capture more complex wall heat flux boundary conditions, McEligot (et. al.) **Equation 2. 12 [26]** and Pfriem's work **Equation 2.13 [27]** include a q^+ parameter **Equation 2.14** to be used in their Nusselt number correlations. Note that q^+ is dependent on the absolute temperature at the inlet and not a temperature difference. While these correlations are less well accepted than Taylor, they do introduce the idea of dependence on both the local radial property variation and the local wall flux level.

$$Nu_b = 0.021 {Re_b}^{0.8} {Pr_b}^{0.4} \left(\frac{T_w}{T_b}\right) exp(-90q^+) \qquad \textbf{Eq. (2.12)}$$

$$Nu_b = 0.027 {Re_b}^{0.8} {Pr_b}^{0.4} (1000 \cdot q^+) \left(\frac{T_w}{T_b}\right)^{-1.4} \qquad \textbf{Eq. (2.13)}$$

$$q^+ \equiv \frac{q''(x)}{\rho_b u_b c_p T_i} \qquad \textbf{Eq. (2.14)}$$

Internal Turbulent Flow in the Developing Region

Chen (et. al.)

In a study conducted by Chen (et. al.), developing turbulent heat transfer in a 2D-duct was investigated **[28]**. The duct geometry had a height of 0.01 m with a length of 2 m. The model used Reynolds-Averaged Navier-Stokes (RANS) equations paired with a 4-equation low-Reynolds number turbulence model to simulate flows of Reynolds number ranging $4560 \leq Re_D \leq 12000$. Chen (et. al.) validated the simulations via a Direct Numerical Simulation (DNS) solving the Navier-Stokes equations for an unsteady flow with a Reynolds number of 3300. The study provided plots for both momentum and thermal parameters of importance such as: U^+ and T^+ vs y^+ **[28, Fig. 1]**, radial profiles of streamwise velocity **[28, Fig. 4]** and skin friction coefficient (C_f) **[28, Fig. 9]** and Nusselt number (Nu_b) **[28, Fig. 10]** vs. axial position. The plots produced by Chen (et. al.) for C_f and Nu_b which can be seen in **Figures 2.1** and **2.2** respectively. These profiles show a "dip" or non-monotonic behavior in the streamwise evolution of both C_f and Nu_b within the developing flow region. This observation will prove to be a central element of the results of the current work.

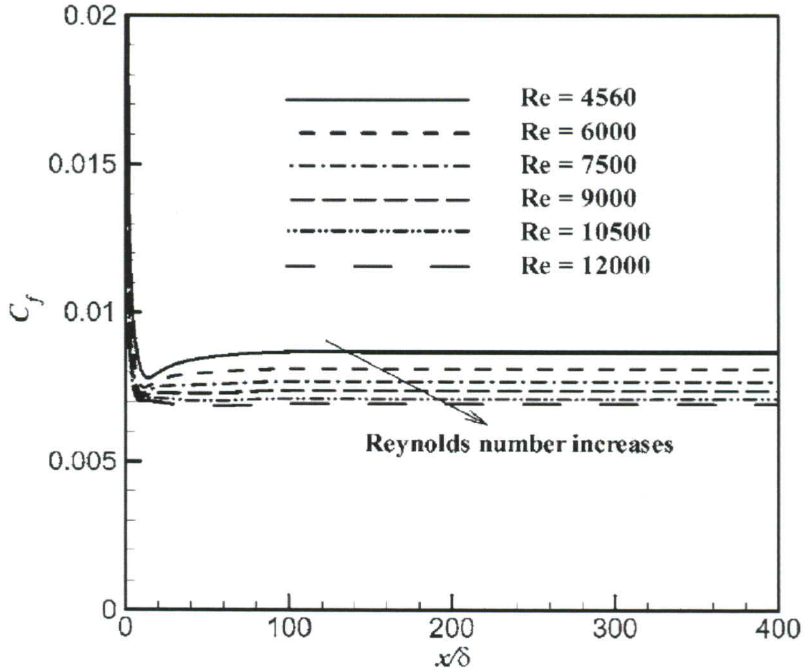

Figure 2.1: Axial Distribution of Skin Friction Coefficient (C_f) ***[28]***

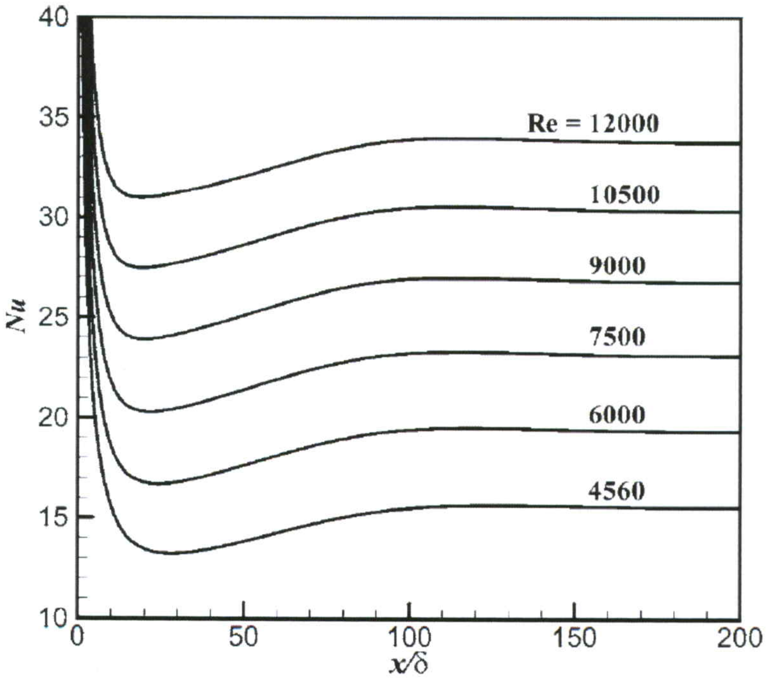

Figure 2.2: Axial Distribution of Bulk Nusselt Number (Nu_b) ***[28]***

Deissler

Deissler's NACA Technical Note (TN) 3016 **[29]** dealt specifically with characteristics of the entrance region of turbulent tube flow heat transfer. The work was comprised of an integral analysis for both uniform wall heat flux and uniform wall temperatures. The analysis was validated by experimental data for Nusselt numbers for air with a uniform wall surface temperature. The plots of the most current interest are Nusselt number vs. axial position $\left(\frac{Z}{D}\right)$ (**Figure 2.3**) and dimensionless temperatures (bulk and wall) vs $\left(\frac{Z}{D}\right)$ (**Figure 2.4**). These results also exhibited non-monotonic axial behavior in the developing region.

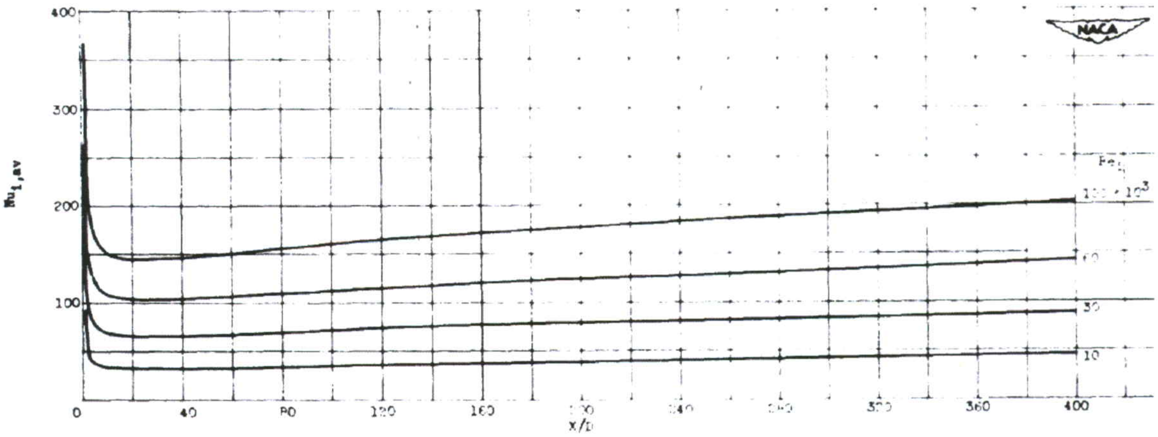

*Figure 2.3: Variation of Average Nusselt Number (Defined by **[29, Eq. 25]**) with Axial Position and Reynolds Number for Gas Flowing in a Tube. Pr = 0.73. Uniform Heat Flux, Uniform Initial Temperature Distribution and Fully Developed Velocity Distribution **[29]***

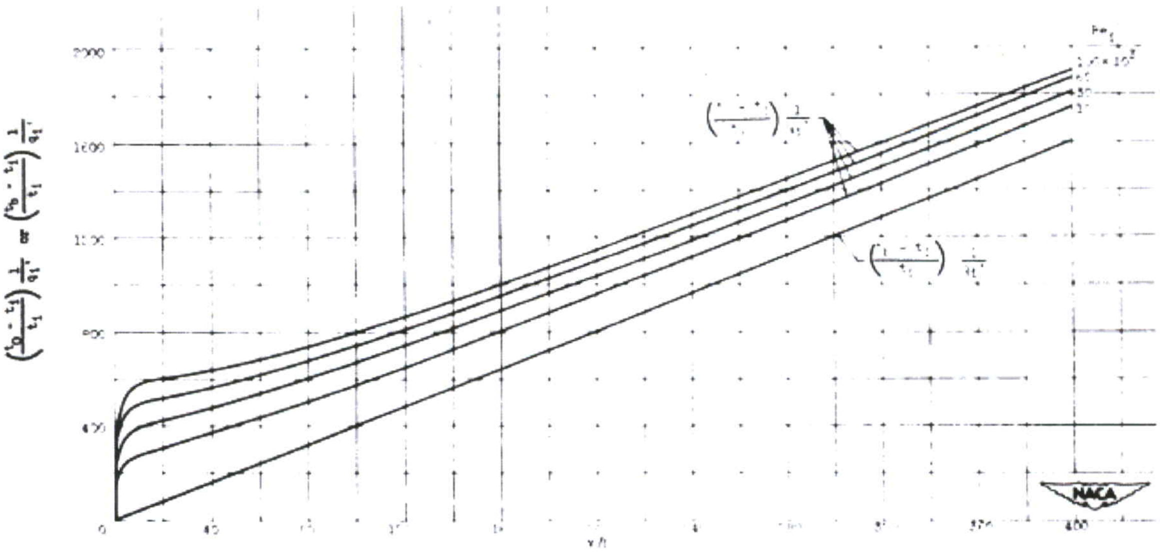

*Figure 2.4: Variation of Dimensionless Wall and Bulk Temperatures with Axial Position and Reynolds Number for Gas Flowing in a Tube. $Pr = 0.73$. Uniform Heat Flux, Uniform Initial Temperature Distribution and Fully Developed Velocity Distribution **[29]***

Similar to TN-3016 discussed above, TN-3145 was comprised of an integral analysis for turbulent heat transfer in smooth tubes **[30]**. The analysis was validated via experimental data that ranged from $0.5 \leq Pr \leq 3000$. The resulting profile of dimensionless temperature (T^+) vs. dimensionless wall distance (y^+) for a Prandtl number of 0.73 (seen in **Figure 4.7**) agrees well with results from the current study as will be discussed in Chapter 4.

Duz

Work done by Duz **[31]** investigates the variation of centerline axial velocity for pipe inlets transitioning to fully turbulent flow. A RANS k-ω SST turbulence model was used to simulate flows ranging from $1000 \leq Re_D \leq 25{,}000$. This was to encompass the regimes for laminar, transitioning, turbulent flow of pipe inlets. The study validated its results via experimental data and standard turbulent wall laws. As with other literature mentioned in this subsection, Duz's work shows a non-monotonic velocity evolution in the developing and transitioning region of the flow **[31, Fig. 7]**.

Doherty (et. al.)

Data collected by Doherty (et. al.) **[32]** from an experimental pipe flow facility at the University of Melbourne discusses an "overshoot" phenomenon in which the centerline velocity accelerates to its maximum when the pipe boundary layers meet, but then decelerates to a final, fully developed, centerline velocity. The facility is comprised of a fan that, from the outlet, sucks air into a cylindrical test section. The section begins with a series of screens and a final circular contraction just upstream of the instrumented pipe flow section. This was done to control flow uniformity and turbulence intensity. The instrumented section's inlet diameter is 9.88 cm with a 15 cm long axial flow "trip" section with 60-grit sandpaper. Overall pipe length is approximately 400 diameters. The facility incorporates a carriage instrumentation mechanism that can move to different axial locations to obtain hot-wire flow recordings at several points traversing the pipe section radially **[32, Fig. 1]**. Experimental results show non-monotonic centerline mean velocity profiles (see **Figure 2.5**) that are qualitatively similar to those computed in the present study (Chapter 4) at entry lengths of $\left(\frac{Z}{D}\right) \approx 60$.

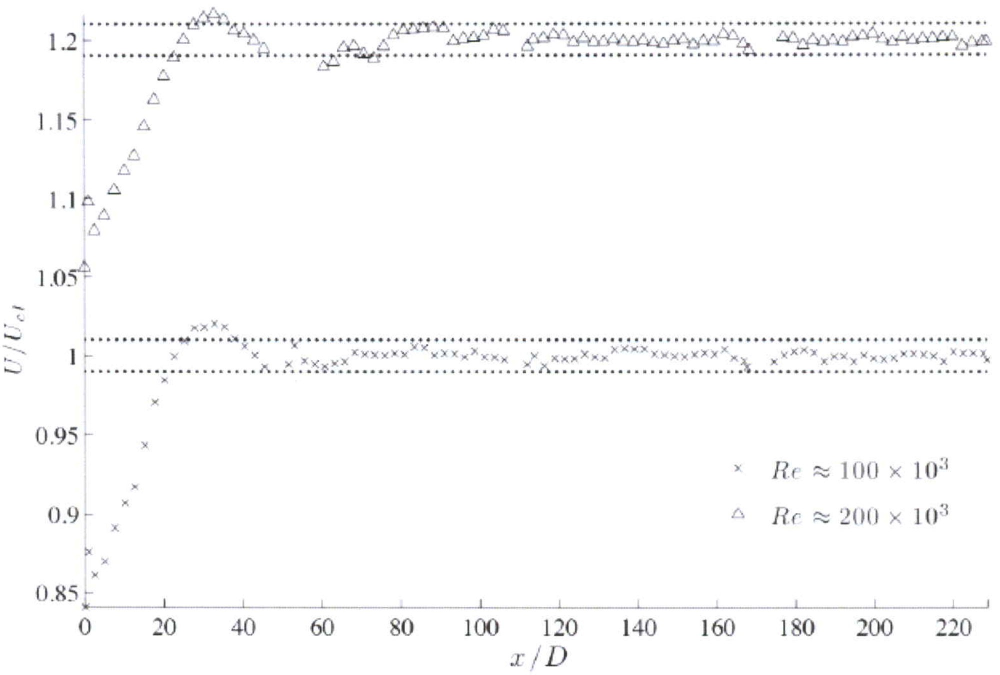

Figure 2.5: Centerline Mean Velocity vs. Axial Position for $Re_D \approx 1x10^5$ *and* $Re_D \approx 2x10^5$ *with* $Re_D \approx 2x10^5$ *Shifted Vertically 0.2 Units for Clarity* ***[32]***

Malik

A dissertation by Malik **[33]** presents results of an investigation into the prediction of heat transfer in both laminar and turbulent flow annular passages. Malik's analysis evaluates three turbulence models: "a length scale equation model," a "bridging model," and a "turbulence kinetic energy model with length scale". The models were validated against various experimental data and showed strong agreement in both radial profiles for velocity and axial development of centerline velocity **[33, Figs. 4.14, 4.15, 4.18-4.20]**, and axial development of skin friction coefficient (C_f) **[33, Fig. 4.24]**. Plots for parameters such as heat transfer rate and Nusselt number are provided as well.

Shown here in **Figure 2.6** is Malik's plot showing the non-monotonic behavior in C_f for the ratio of outer to inner radius of 0.99. This result is interesting as it shows three different computational models and two experimental data sets producing a non-monotonic C_f for a two-dimensional channel flow.

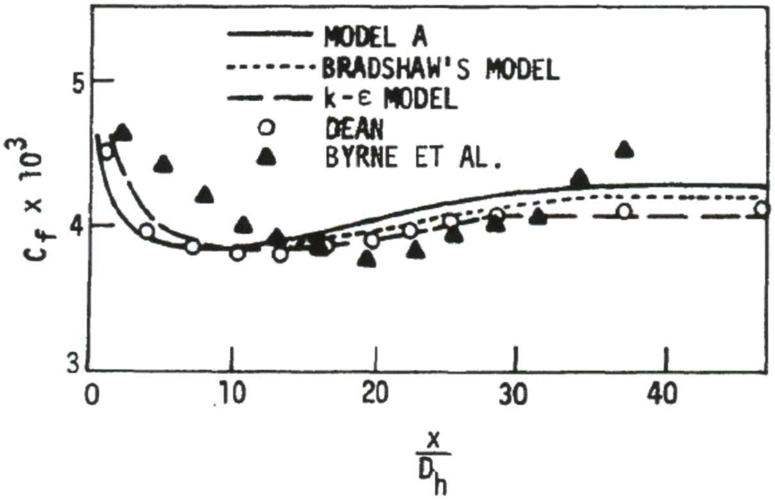

*Figure 2.6: Predicted Distribution of Skin Friction Coefficient in an Annulus with ratio of outer to inner radius of 0.99 Compared with the Results for a Parallel Wall Duct **[33]***

Supercritical Flows

Youn and Mills

A CFD study of turbulent supercritical hydrogen in uniformly heated circular tubes was conducted by Youn and Mills **[22]**. The intent was to investigate a supercritical hydrogen flow exposed to wall heat fluxes as high as 1.1 x 10^7 W/m^2 in applications to the cooling of critical elements of hypersonic aircraft. Youn and Mills used a Reynolds Averaged Navier-Stokes (RANS) *k-ε* two equation viscosity model with a low-Reynolds number wall function. The work took material properties for hydrogen very near the critical temperature and pressure (hydrogen critical point: 33.145 K, 1.296 MPa **[34]**) into account and presents the large changes in thermophysical properties to reader. They used the same material property source for supercritical hydrogen as was used in the current work. Youn and Mills considered flows at cryogenic hydrogen temperatures and at Reynolds numbers on the order of 1.1 x 10^6 and found that the Taylor correlation was the best fit to their results. Their results exhibit non-monotonic radial velocity profiles. However, they do not show non-monotonic behavior of the Nusselt number in contrast to the other studies reviewed above.

Dang, Zhong (et. al.)

Dang, Zhong (et. al.) conducted a CFD study of kerosene flowing through an axisymmetric, horizontal tube of 2 mm in diameter. The mass flow rates varied from 1.5-15 gm/s with a wall heat flux of 0.15-2.0 MW/m2 **[35].** The study incorporated a model of the material properties of RP-3 aviation-grade kerosene and used a two-layer RNG k-ε RANS model along with the Wolfstein turbulence model for the near-wall region. The model geometry consisted of a 1 m long tube. 0.1 m of which was to be an unheated start, developing region with the following 0.9 m having a uniform flux wall heat boundary condition. As liquid kerosene transitioned to a supercritical state, a noticeable rise in both velocity and Reynolds number occurred. The study found a complex behavior of the convective heat transfer coefficient as the thermodynamic state of the fluid passed near the critical point. This study is quite different from the present work in that the present interest, the thermodynamic state of the fluid is never near the critical point.

Locke and Landrum

Locke and Landrum **[36]** reviewed a number of Nusselt number correlations, thermophysical data tables and experimental studies of heated tube flows. They conducted an uncertainty analysis on these Nusselt number correlations. They note a large disagreement in supercritical hydrogen material properties supplied from various references. The material property data tables alone had uncertainty values upwards of 10%. The review mentions multiple studies conducted from 1959-1968 focusing in both cryogenic regenerative cooling temperatures for LOX/LH2 chemical propulsion and high-temperature environment studies for work in areas such as fissionable nuclear propulsion.

Nuclear Thermal Rocket (NTR) Fuel Element Models

Cheng (et. al.)

Cheng (et. al.) **[37]** in 2007 developed a CFD model specifically for use with a single UC-C-ZrC NTR fuel test element. The work consisted of two numerical models including both solid and fluid domains and coolant passages that were 2.05 mm in diameter. The work incorporated a RANS k-ε viscosity two-equation model along with a heat conjugate thermal model to couple the fluid and solid heat transfer domains.

The following information used for Cheng (et. al.) was supplied to them by Dr. Bill Emrich (et. al.) **[37, Pg. 14].** A half-cosine power profile down the length of the passages was used.

Simulations developed by Cheng (et. al.) in 2013 **[38]** were created to analyze reactor chamber heat transfer efficiency and to explore fuel element corrosion and mass losses exhibited during the original NERVA testing. The individual fuel elements were hexagonal in shape, 19 mm flat to flat, with 19 extruded coolant channels (with 3-

nonexplicitly stated diameters) and 890 mm in length. The model of interest was a 60° slice of the total element to save computational resources. Cheng (et. al.) included the hydrogen fluid flow, inner coolant channel wall coating material (U, Zr)C, and the solid (U, Zr)C-graphite composite (materials taken from legacy NERVA engine designs). In total, the model was 4.5 million cells in a hybrid unstructured grid form with structured layers for the turbulent boundary layer and near coolant channels. A conjugate heat transfer model simulated the wall coating and solid fuel portions of the model with a *k-ε* turbulence model for the turbulent hydrogen flow and fluid heat transfer. Three different simulated reactor axial/radial power profiles were investigated.

The study concluded that under the worst design conditions (smallest diameter channels, thus largest $\left(\frac{Z}{D}\right)$, cosine-cosine power profile), the flow tended to choke, and form localized hot spots within the solid fuel element. Any addition of heat flux led to a hydrogen mass flow reduction. This was the proposed causation for mid-section corrosion and mass losses.

Appel

The study conducted by Appel **[39]** was to determine the capability CFD modeling had to simulate NTR fluid flows and heat transfer. The primary fuel element simulated was 1.4 m in length with cooling channel diameters ranging from 1.2 to 2.4 mm. The CFD portion of the study reviewed four different RANS models to determine which obtained the best fit to experimental data results. The study included the *k-ε* 2-layer realizable model, the *k-Ω* SST Menter model, *k-ε* AKN model and *k-ε* V2F model. After conducting a mesh validation process and comparing to experimentally collected data, Appel concluded that the k-ε realizable 2-layer model was the best mix between result accuracy, model stability and dependency on first cell y^+ locations.

The values for specific heat, thermal conductivity, and dynamic viscosity were all determined to have very little variation due to pressure and were model as trendlines dependent on local temperature only. The study mentions the importance of large density variations; however, the study does not explicitly state its method for handling density variations within the CFD model itself.

The study considered three mesh types to be used for the final simulation including polyhedral, tetrahedral and a trimmer mesh. The polyhedral meshing method was used for its fast meshing time and ability to run in parallel mode for Star-CCM+ software at the time of the study. Appel found that the realizable k-ε model was the least sensitive to first-cell y^+ mesh sizing where the k-ε V2F model solution deviated rapidly when first-cell y^+ exceeded 1.04. This is an important consideration with overall mesh domain size and computational expenses in mind.

Webb (et. al.)

Research conducted by Webb et. al. **[40]** was to determine the best cooling channel surface-area-to-volume ratio for the XNR-2000 reactor configuration. For more information on the XNR-2000 NTR reactor design, see work by Peery (et. al.) **[41]**. The model not only included the cooling channel flow, it also simulated the solid core material (like Cheng (et. al.) **[37], [38]**) and outer reactor control drums seen in a NTR. The numerical domain included a 0.2 m Beryllium Oxide (BeO) reflector section doubling as an unheated starting length for flow development in the cooling channels followed by a 0.7 m length of W-UO_2 CERMET fuel. The model also included a 0.25 mm thick W-25Re cladding on the inner walls of the coolant channels. Simulation runs were limited to 12 hours for both meshes analyzed (on the order of 30-40 million mesh cells). The simulation used "core thermal-hydraulic optimization" to account for temperature dependent material properties.

Walton

The NASA technical memo published by Walton in the fall of 1992 describes a code to model the thermal-hydraulic characteristics of solid core NRX NTR reactor fuel elements cooling channels. The code took user inputs for geometry and axial heat generation profiles to compute values such as fluid temperatures, wall temperatures and pressure profiles **[42]**.

The work included is its own literature survey comparing classical form Nusselt number correlation equations developed for NTR or supercritical tube flows. The survey agreed with the Nusselt number correlation survey discussed previously in Chapter 2. Walton compared the model's code outputs to actual NERVA NRX data. The data and boundary conditions confirmed the current studies conditions were generally in comparable ranges for the NTR-like flows found in NTREES.

Conclusions on Past Works

The current study draws in works from multiple different areas of scientific research including: the transition to turbulence in internal flows, large scale experimental testing such as the NERVA program, small scale heated tube flow tests, supercritical hydrogen material property evaluations, Nusselt number correlation development and lastly, numerical simulations of supercritical fluid tube flows. The works listed in the sections above may not match the current study's conditions or requirements exactly, but, they provided insight into many questions that arose during various stages of the current study.

The project at hand generally revolves around work such as NERVA and NTREES. However, fundamentally, it is a numerical model of supercritical turbulent tube flow with high wall heat flux levels. Studies such as those by Youn/Mills, Dang/Zhong (et. al.) match this fundamental description very closely. The choice for the best source for material properties (McCarthy **[34]**) was validated independently by Youn/Mills, Appel and Webb. The unexpected "dip" or non-monotonic developing flow region temperature, velocity and Nusselt number profiles results discussed in Chapter 4 are, to one extent or another, seen in works by: Diessler, DUZ, Doherty, Chen, Malik Youn/Mills, Webb (et. al.), Cheng (et. al.) and Dang/Zhong (et. al.). Finally, the development of Nusselt number correlations for turbulent flows, including those dealing with large variations in material properties in supercritical fluids such as hydrogen, provide aid for future work in the areas of supercritical fluid heat transfer in internal turbulent flows.

CHAPTER 3

Methodology, Numerical Domain, Setup and Model Validation

This chapter will define the methodology and principles used in the setup, running and validation of the numerical simulations of a turbulent flow of supercritical hydrogen at heat flux levels and channel dimensions taken from the NTREES fuel element. First, the physical geometry, numerical domain and values of the parameters of interest will be discussed. Next, the User Defined Function (UDF) code required to manage the thermophysical properties and model boundary conditions for supercritical hydrogen will be described. Then, governing equations will be described. After that, the domain meshing and mesh validation are presented. Finally, the CEL (CFX Expression Language) code written for the ANSYS CFD-Post (Processor) software to export flow data and further post processing in Excel will be covered.

Physical Geometry of Model

The physical geometry of a NTREES hexagonal fuel rod test element can be seen in **Figure 3.1.** The elements are, as stated previously, comprised of sintered Tungsten. They are 40.64 cm in length, 1.905 cm flat to flat with 7 extruded propellant coolant channel tubes each having a diameter of 0.381 cm. The channels are spaced such that when orientated into a bundle, each hole is equal distance from any adjacent hole, even if the adjacent hole is in another fuel rod. The current work focuses on a model of heat transfer into the propellant flowing through a single coolant channel tube. This is the defined numerical domain of this investigation.

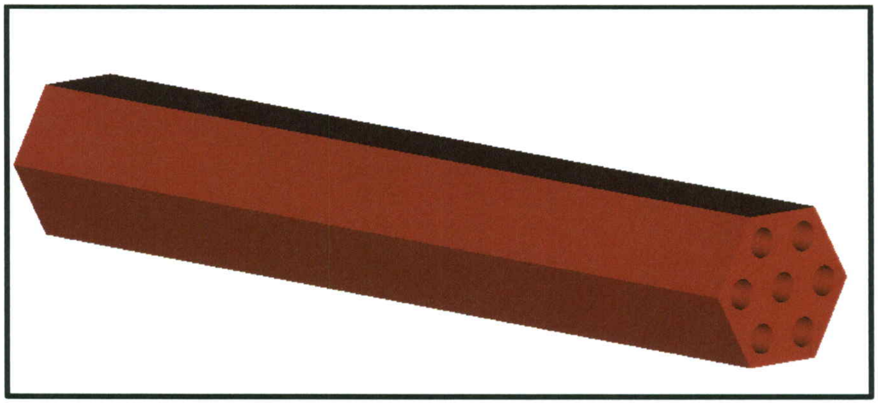

Figure 3.1: NTREES Sintered Tungsten Hexagonal Fuel Element

Parameters and Values of Interest

Parameters involved with possible and known failure modes of NTREES fuel rods were selected by Dr. William Emrich for this study **[34]**.

- Tube diameter of 3.81 mm and tube length of 406.4 mm
- Inlet mass flux: Mass flux varied from 185-425 kg/m^{2}s depending on which simulation was being conducted and was defined in the boundary conditions section of the UDF code.
- Inlet hydrogen temperature: Inlet fluid temperature was set to 300 K within the boundary conditions section of UDF code.

- Inlet hydrogen pressure: Inlet hydrogen pressure was set to ensure that the boundary conditions selected for each simulation do not over constraint the simulation solution.
- Inlet Reynolds number: The Reynolds number (**Equation 2.4**) was monitored to insure simulations remained in the turbulent flow regime ($Re_D \geq 4000$). Typically, $70{,}000 \leq Re_D \leq 80{,}000$.
- Inlet Prandtl number: $Pr \cong 0.68$ for hydrogen at the simulation temperatures and pressures (Prandtl number is defined by **Equation 2.5**).
- Limit on fuel element channel wall temperature: The fuel element of the current study is comprised of sintered tungsten. The melting point of Tungsten is 3680 K, so channel wall temperatures must be below this value **[43]**. The current study was to target an exit channel wall temperature around 2500 K.
- Exit fluid velocity: From information provided on the NTREES facility, it was known that an exit velocity of 700 m/s was to be achieved **[9]**.
- Supercritical hydrogen material properties: A major feature of this study is the implementation of supercritical hydrogen material properties into the simulation.

The basic elements of the simulation outputs are introduced here:

- Streamwise bulk fluid temperature or mixing-cup temperature: The bulk fluid temperature is the mass-flux-weighted average fluid temperature across the tube at a given streamwise position. As such, it represents the enthalpy content at a given cross-section of tube. The bulk fluid temperature is the standard reference temperature for computing the heat transfer coefficient and the Nusselt number denoted as Nu_b. This value is computed by a custom program written using CFX

Expression Language (CEL) code for ANSYS-CFD-Post as **Equation 3.1** where φ would be temperature **[44]** and the integral is across the tube cross-section.

$$\frac{\int \varphi\rho|\vec{v}\cdot d\vec{A}|}{\int |\vec{v}\cdot d\vec{A}|} = \frac{\sum_{i=1}^{n} \varphi|\vec{v}_i\cdot \vec{A}_i|}{\sum_{i=1}^{n} \rho_i|\vec{v}_i\cdot \vec{A}_i|} \qquad \textbf{Eq. (3.1)}$$

- Expected Thermal-Entry-Length: A calculation was performed of the thermal development length for the inlet Reynolds number and Prandtl number for a constant-property flow at a uniform flux boundary condition **[45].** The procedure involves a series solution to the "turbulent Graetz problem." The solution yielded $\left(\frac{Z}{D}\right) \approx 60$ for full thermal development for the parameters selected above. See **Figure 3.2** for a plot of the ratio of the local Nu_b to the fully developed Nu_b from the turbulent Graetz solution. It should be noted; this solution was conducted without the 5% unheated starting length that is present in all CFD simulations discussed in Chapter 4. The turbulent Graetz problem was simply a means to preliminarily estimate the thermal entry length.

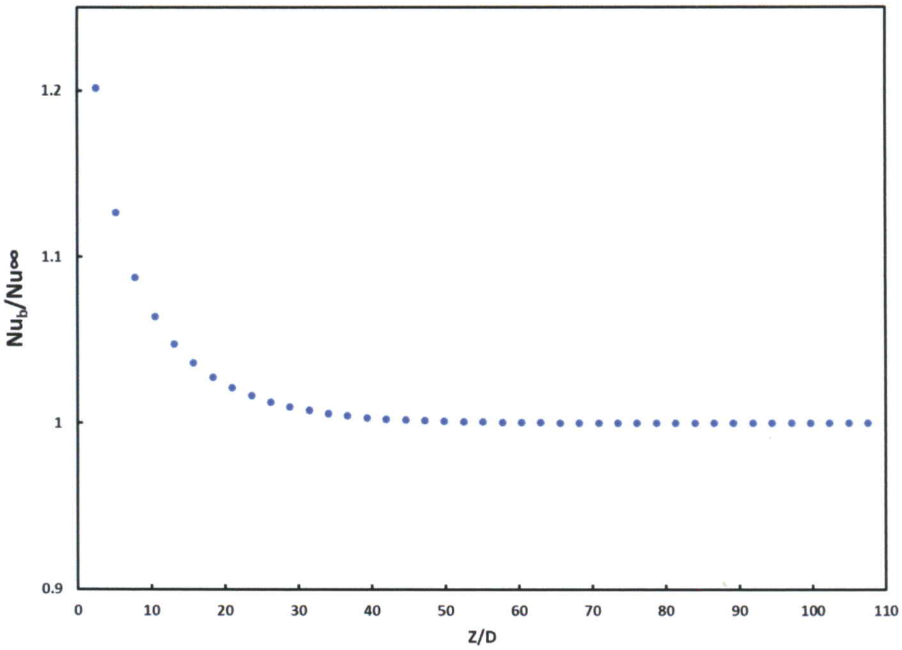

Figure 3.2: Solution to the Turbulent Graetz Problem for NTREES' Flow Parameters

- Nusselt number: The local Nusselt number is obtained by first solving for the local heat transfer coefficient from the user input heat flux and the computed wall and bulk fluid temperatures using **Equation 3.2**. Then, by plugging the heat transfer coefficient, pipe diameter and fluid thermal conductivity into **Equation 2.1** one obtains the Nusselt number.

$$h_c \equiv \frac{q"}{(T_w - T_b)} \qquad \textbf{Eq. (3.2)}$$

User Defined Function Code

For a user to simulate more complex flows and get the most out of the ANSYS software package, ANSYS-Fluent has the User Defined Function (UDF) facility **[46]**. This facility is a c-code language-based system that allows users to customize model boundary conditions, implement specific commands, assign variable material properties and export specific data or custom flow variables otherwise unavailable. The facility requires users to write code within the "DEFINE" macros using pre-existing sub-function commands calls. These pre-written Macros allow for a much more streamlined coding process; however, they can be limited in ability at times. The user-written code functions can be then accompanied by header files compiled inside a source code library folder via the ANSYS-Fluent GUI (Graphic-User Interface). The functions are then *hooked* to their designated macros inside the ANSYS-Fluent's GUI.

The current study incorporated the: PROFILE, PROPERTY and SPECIFIC_HEAT pre-existing UDF sub-function calls to aid in defining custom boundary conditions and variable fluid material properties. The define macro DEFINE_PROFILE was used to apply custom boundary profiles for: inlet mass flux, inlet temperature, wall heat flux, outlet pressure and outlet backflow temperature. The calls DEFINE_PROPERTY and DEFINE_SPECIFIC_HEAT were used in the handling of local cell variable material properties. More information on model boundary conditions and methodology for accurately defining material properties will be discussed in further detail in the sections to come.

Thermophysical Material Properties

The material properties for supercritical hydrogen at the temperatures and pressures required in this study were introduced into ANSYS-Fluent via custom coding through Fluent's UDF facility. This effort was a significant enabling accomplishment in performing these simulations.

The choice of hydrogen as a propellant is two-fold. First, it has an exceptionally low molecular weight. To understand this strong suit, the parameter specific impulse (I_{sp}) must be described. Specific Impulse, as seen in **Equation 3.3**, is how much thrust per unit of propellant mass flow rate a propulsion system generates **[1]**. I_{sp} is proportional to the square root of the propellant total temperature over its molecular weight **[1]**.

$$I_{sp} g_c = \sqrt{\frac{2\gamma R T_c}{(\gamma-1)M}\left[1 - \left(\frac{P_e}{P_c}\right)^{\frac{\gamma-1}{\gamma}}\right]} + \frac{P_e A_e}{P_c A_t}\sqrt{\frac{R T_c}{\gamma g_c \left(\frac{2}{\gamma}+1\right)^{\frac{\gamma+1}{\gamma-1}}}} \qquad \textbf{Eq. (3.3)}$$

The second property hydrogen possesses as a propellant choice is its specific heat capacity which is around 14 times that of most gases. This makes it an exceptional transporter of thermal energy from the fuel elements to be exchanged for thrust in a NTR.

The downside of this is material properties of supercritical hydrogen at the delivery pressure used in an NTR vary substantially with a change in temperature. The term "spin isomer" is the H_2 nucleus spin orientation with respect to the axis perpendicular to the molecular axis itself **[47]**. This means there can be two potential spin isomers: one in which the spin axes are parallel called "Parahydrogen" and one in which they are antiparallel called “Orthohydrogen”. Each spin isomer of the H_2 exhibits different thermophysical material properties. Above 300 K, hydrogen is made up of predominantly a 25% Parahydrogen and 75% Orthohydrogen mixture and is generally stable at this ratio within the temperature ranges in the investigated flow. This mixture ratio in most readings is coined “Normal Hydrogen”. It should be noted that the dissociation of hydrogen at high temperatures was accounted for by using experimental data for the material properties. This insures that at high temperatures, when hydrogen starts becoming monotonic, the material properties reflect this thermodynamic characteristic. Provided in **Figure 3.3** is a *T-s* diagram for hydrogen reaching temperatures upwards of 3000 K. Flows investigated in the current study, which reach around 2500 K at 3-4 MPa, will reside far above the saturation dome and critical point, well within the supercritical fluid domain.

Figure 3.3: Hydrogen T-s Diagram Extending to Regions Upwards of 3000 K ***[2]***

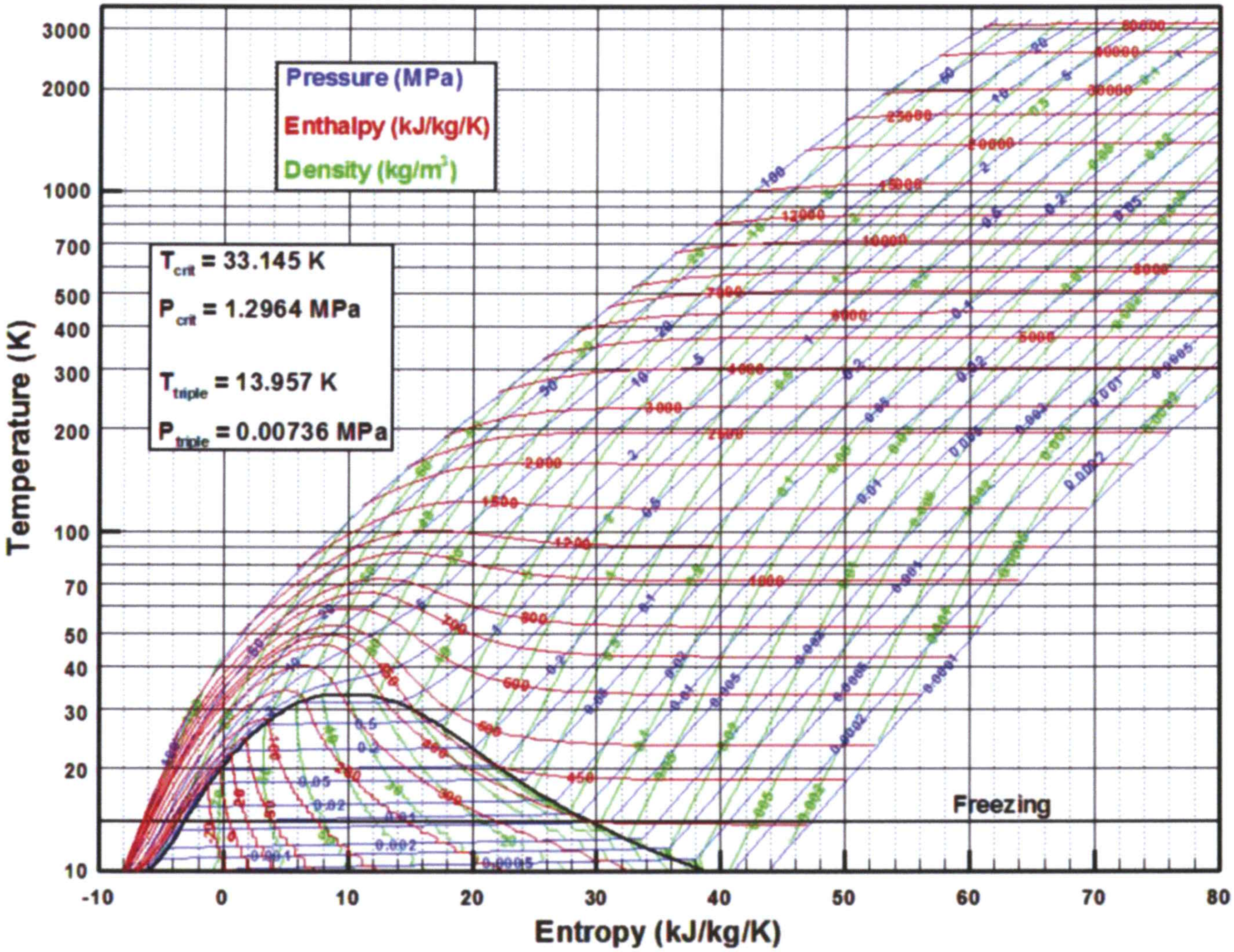

Hydrogen Material Properties Evaluated Via Temperature Dependent Trendlines

During the initial search for creditable sources of high temperature Normal Hydrogen data, The National Institute of Standards and Technology (NIST) resources and references were reviewed as a starting point. Sources used for their tables and equations of state were compared to sources used in similar research discussed in Chapter 2 to insure they were sufficient for the needs of the current study. The primary-source data presented by McCarty (et. al.) **[34]** were selected. These experimentally derived data tables were then exported into an Excel workbook and inspected. It can be shown that normal hydrogen exhibits very little variation due to pressure for dynamic viscosity, thermal conductivity, specific heat at constant pressure and speed of sound. For the primary pressure range of the study, 3.10-7.10 MPa, the largest change (18.3%) occurred in thermal conductivity along the 3000 K isotherm. This is a much higher temperature than the channel wall or fluid are to achieve. The change is reduced to less than 1% difference for pressure and temperatures produced by the NTREES simulations. Thus, it was deemed acceptable to create best fit polynomial trendlines varying as a function of temperature only for these properties.

The developed trendlines for dynamics viscosity (**Figure 3.4**), speed of sound (**Figure 3.5**), thermal conductivity (**Figure 3.6**) and specific heat at constant pressure (**Figure 3.7**) can be found on the pages to follow.

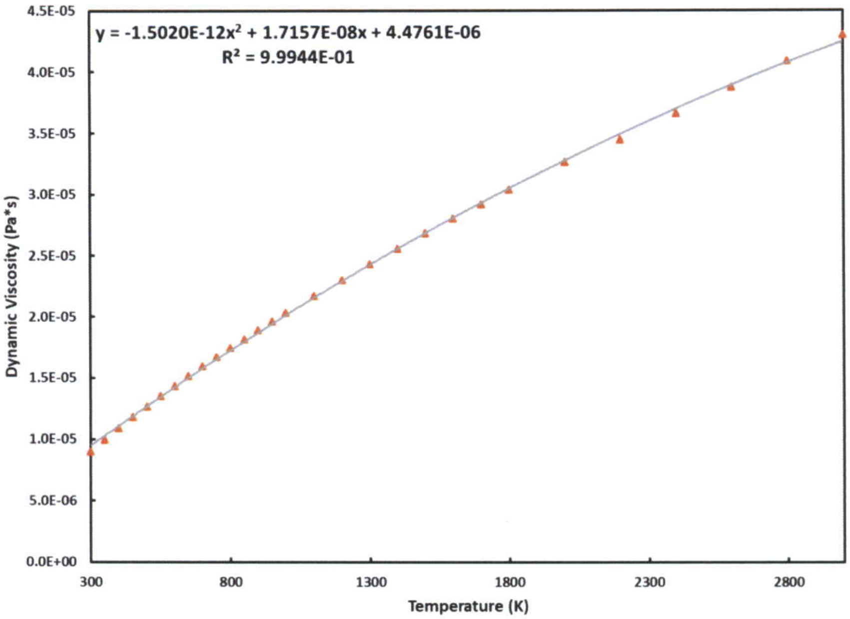

Figure 3.4: Hydrogen Dynamic Viscosity Trendline for Temperatures Ranging 300-3000 K

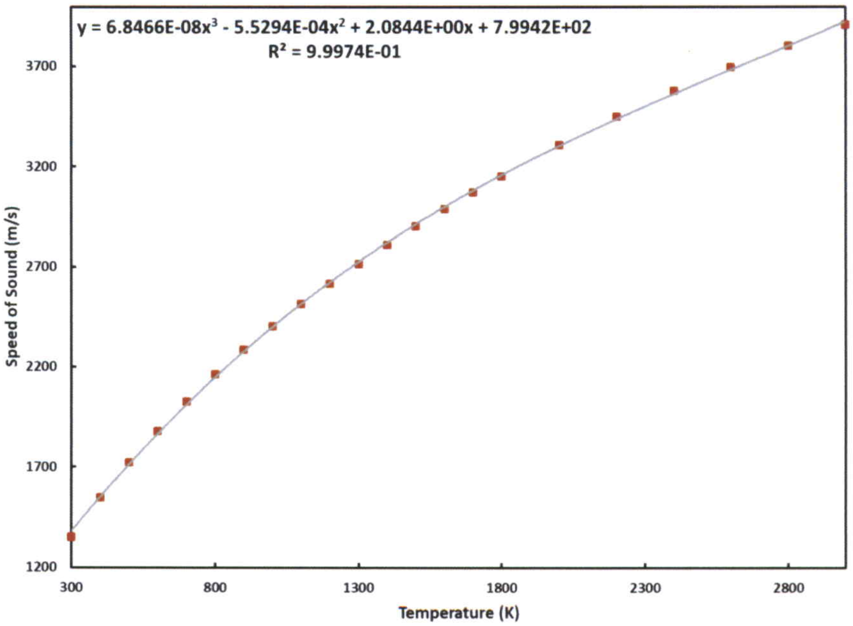

Figure 3.5: Hydrogen Speed of Sound Trendline for Temperatures Ranging 300-3000 K

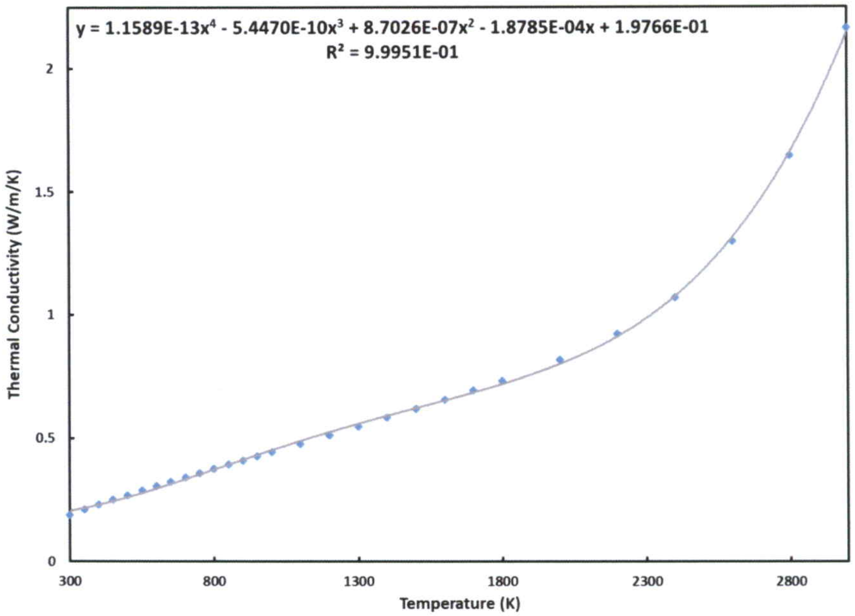

Figure 3.6: Hydrogen Thermal Conductivity Trendline for Temperatures Ranging 300-3000 K

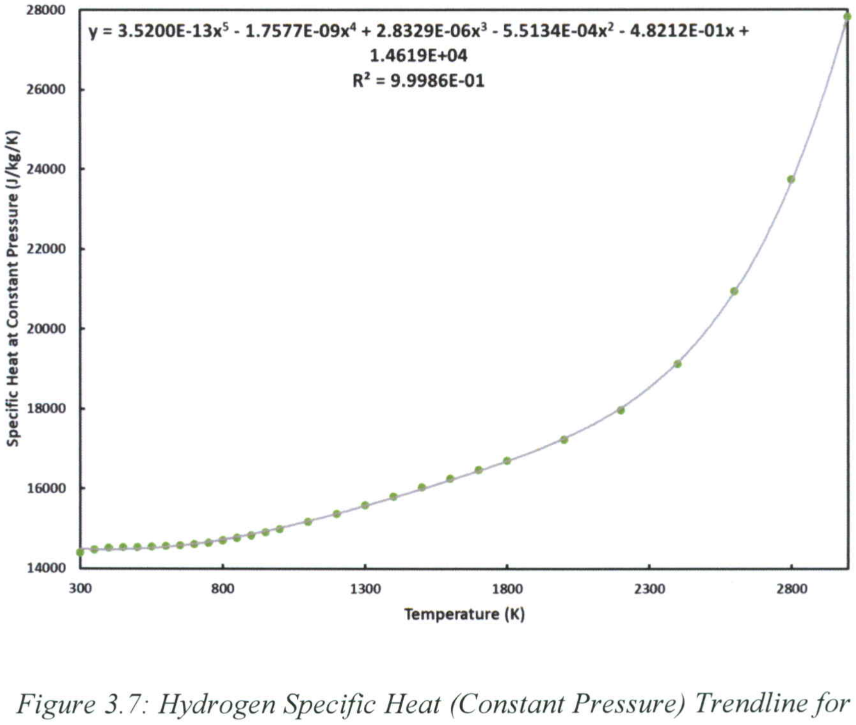

Figure 3.7: Hydrogen Specific Heat (Constant Pressure) Trendline for Temperatures Ranging 300-3000 K

The material property trendlines were then implemented via the UDF facility code DEFINE_PROPERTIES and DEFINE_SPECIFIC_HEAT function calls. Coding was set up to call for local cell centroid pressures and temperatures from ANSYS-Fluent. The commands were executed for every iteration in the simulation. The code read this information, determined if the incoming values were valid and within a pre-defined pressure/temperature range and then inserted local temperature into the associated trendline equations to obtain local cell material properties to be then passed back to ANSYS-Fluent to use in solving the current iteration of the simulation.

Hydrogen Density with Varying Pressure and Temperature

Density was shown to be the only material property modeled that varied substantially due to both pressure and temperature. This dual variation was handled by a 2D matrix look up table header file and bilinear interpolation integrated into the UDF code sub-function command file to obtain the best density resolution at any specific local cell flow conditions. **Figure 3.8** shows the bilinear interpolation section of the DEFINE_PROPERTIES sub-function command to implement locally varying fluid density. The 2D look up table ranged from 300-3000 K and 0.10-7.10 MPa. The values of density have an exponential decay trend with increasing temperature and were plotted in increments of 0.5 MPa isobars seen in **Figure 3. 9**.

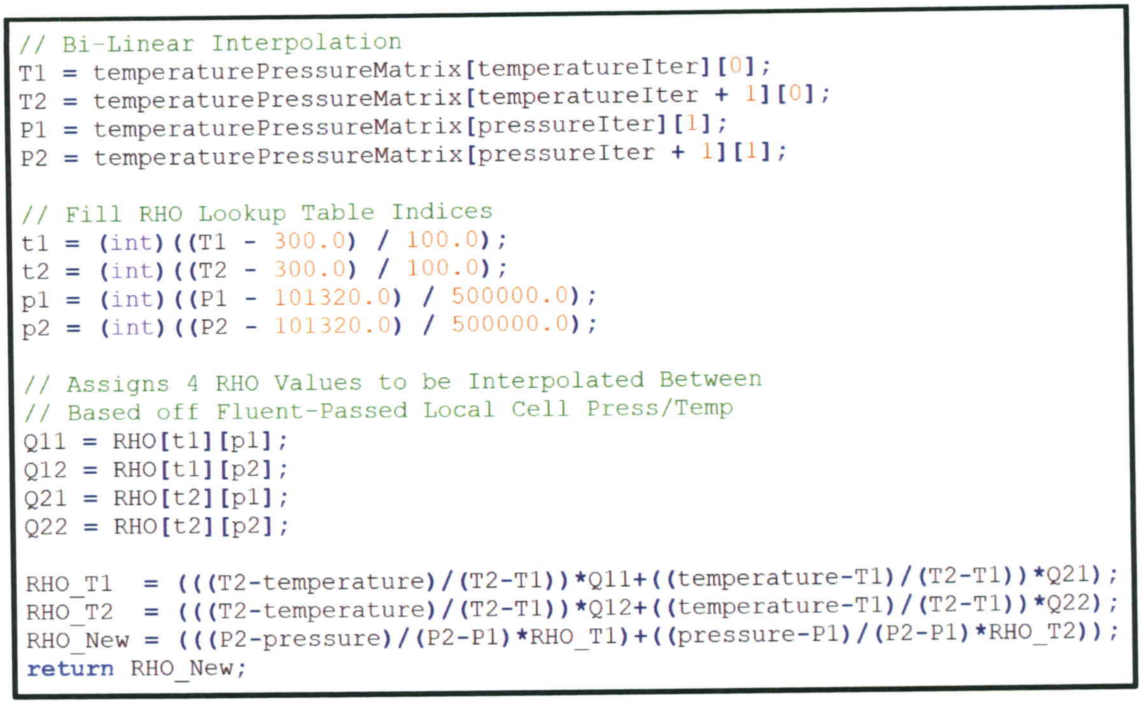

```
// Bi-Linear Interpolation
T1 = temperaturePressureMatrix[temperatureIter][0];
T2 = temperaturePressureMatrix[temperatureIter + 1][0];
P1 = temperaturePressureMatrix[pressureIter][1];
P2 = temperaturePressureMatrix[pressureIter + 1][1];

// Fill RHO Lookup Table Indices
t1 = (int)((T1 - 300.0) / 100.0);
t2 = (int)((T2 - 300.0) / 100.0);
p1 = (int)((P1 - 101320.0) / 500000.0);
p2 = (int)((P2 - 101320.0) / 500000.0);

// Assigns 4 RHO Values to be Interpolated Between
// Based off Fluent-Passed Local Cell Press/Temp
Q11 = RHO[t1][p1];
Q12 = RHO[t1][p2];
Q21 = RHO[t2][p1];
Q22 = RHO[t2][p2];

RHO_T1  = (((T2-temperature)/(T2-T1))*Q11+((temperature-T1)/(T2-T1))*Q21);
RHO_T2  = (((T2-temperature)/(T2-T1))*Q12+((temperature-T1)/(T2-T1))*Q22);
RHO_New = (((P2-pressure)/(P2-P1)*RHO_T1)+((pressure-P1)/(P2-P1)*RHO_T2));
return RHO_New;
```

Figure 3.8: UDF Code Section for the Bilinear Interpolation of Local Pressure/Temperature to Produce Locally Varying Hydrogen Fluid Density

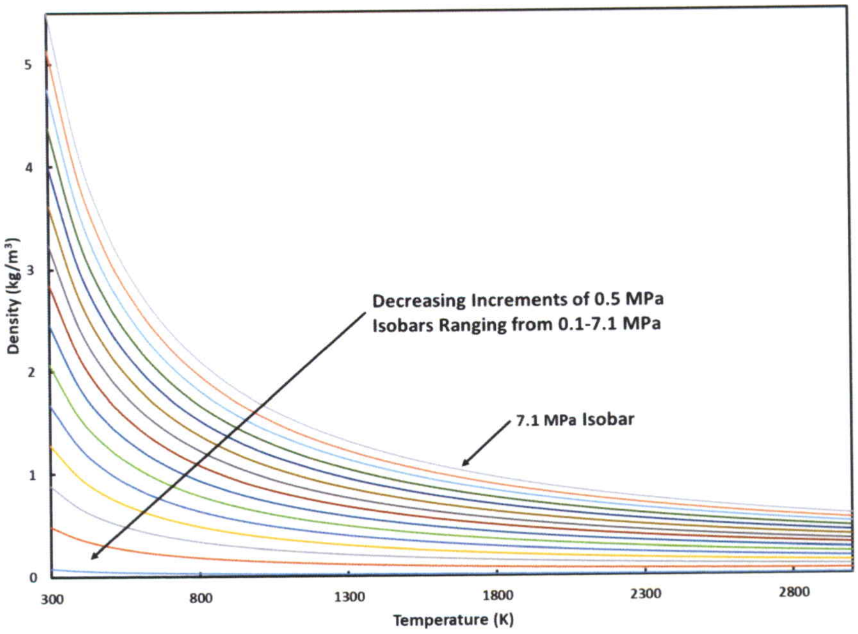

Figure 3.9: Hydrogen Density Isobars from 0.01-7.10 MPa for Temperatures Ranging 300-3000 K

As stated previously, the 2D matrix look up table for density was implemented via a separate header file to act as a more modular simulation setup. This means, if a user wanted to switch to different propellant type (e.g. from hydrogen to helium), they simply would modify the 2D data matrix and update the propellant trendlines leaving the master UDF file structure alone. The local density material property bilinear interpolation was then implemented via the UDF facility code DEFINE_PROPERTIES function call. Coding was set up to call for local cell centroid pressures and temperatures from ANSYS-Fluent. The commands were executed for every iteration in the simulation. The code read this information, determined if the incoming values were valid and within the pre-defined pressure and temperature range. Then, the code inserted the local pressure and temperature into the associated indices (t1, t2, p1 and p2 seen in **Figure 3.8**) to determine local densities from the 2D matric look up table. Finally, these density values were placed in the bilinear interpolation equations to obtain local cell density to be then passed back to ANSYS-Fluent to use in solving the current iteration of the simulation.

Boundary Conditions

The parameter range of the NTREES facility as it informs this study was presented earlier in this chapter. No finer details were specified as it was expected that the model be robust enough to simulate any number of flow conditions within the described range. This led to an extensive process of ramping boundary conditions such as mass flux and heat flux up to reach the specified wall temperature and velocity at the element's exit. The tube exit pressure was fixed at 3.06 MPa, and the inlet pressure was determined by the mass flow rate and the wall heat flux for each run. The 3.06 MPa was determined from the various literature on NTR exit conditions and past works discussed in Chapter 2.

The implementation of the various boundary conditions, material properties and data overflow protection were done by UDF code commands. The code was set up such that it could be scaled up to incorporate both fluid and solid numerical domains. The primary goal of the UDF code was for an outside user to be able to easily modify boundary conditions and material types (e.g. switching the propellant type from hydrogen to helium) without editing of the master code structure. The user would need to change any input boundary condition values, select the correct wall heat flux flag for the uniform or cosine wall flux profile desired and if a propellant type change is required, replace the property trendlines and material header file with one containing the correct look up table. See **Figure 3.10** for the "inputs" section of the UDF code file.

```
/******************************************************************************
    Flags
******************************************************************************/
real flagFlux    = 1;   // If 0, Flux = Constant. If 1, Flux = Eq. 9.32 [2]
real flagRHO     = 1;
real flagMU      = 1;
real flagCP      = 1;
real flagK       = 1;
real flagSpd_Snd = 1;
/******************************************************************************
    Global Variables
******************************************************************************/
extern real RHO[28][15];               //Indices [temperature][pressure]
extern real temperaturePressureMatrix[28][2];
/******************************************************************************
    Model Parameters
******************************************************************************/
real tempIn             = 300;      //(K)
real massFluxStart      = 185;      //(kg/s/m2)

real tempOut_BFFinal    = 2500;     //(K)    ***Back Flow Temperature***
real pressOut_Final     = 3006325;  //(Pa*s)

real tempValid          = 600;      //(K)    ***Used for Mat Props Functions
real pressValid         = 101325;   //(Pa)      Insures real data values exist
                                    //          for function looping***

real qDotFluxScalar     = 3750000;  //(W/m2) ***Used for Pave Eq. 9.32 of [2]
real scalePara          = 3.3;      //          Alpha in 9.32
real locationPara       = 1.05;     //          L in 9.32***
                                    //
                                    //       ***NOTE: qDotFluxScalar = qFlux
                                    //                for Constant Flux Cases***
/******************************************************************************
```

Figure 3.10: Model Flag and Boundary Condition Parameters Input Sections for UDF Code

Constant Material Properties, Uniform Heat Flux Boundary Conditions

The uniform wall heat flux boundary condition and uniform material properties were selected to facilitate validation of mesh sizing and overall model. The outlet pressure was set to the 3.06 MPa, constant material properties were referenced from 3.10 MPa. The reference temperature was selected to be 1100 K, the midrange value knowing an inlet temperature of 300 K and a maximum outlet temperature of 2500 K. Once a stable ratio of mass flux and wall heat flux was established, the ratio was scaled up until an outlet wall temperature near 2500 K was achieved (In practice, this value fell between 2260-2300 K depending on the selected mesh resolution).

Constant Properties, Uniform Wall Heat Flux:

- Inlet:
  - $\mathrm{Re}_D = 74{,}727$
    - Constant material properties, therefore, constant Re_D
  - $\mathrm{T}_{Inlet} = 300\ \mathrm{K}$
  - $\dot{m} = 4.85\ \frac{gm}{s}$
- Outlet:
  - $\mathrm{P}_{Outlet} = 3.06\ \mathrm{MPa}$
- Wall:
  - $q''_{Wall} = 17.0\ \frac{\mathrm{MW}}{\mathrm{m}^2}$
  - 5% unheated start

The addition of a 5% unheated starting length to all simulation runs allowed the momentum boundary layer a short development prior to exposing the flow to the very high heat fluxes that characterize this work. Without this unheated start, runs with variable properties tended to be unstable in the developing/transitioning portion of the tube.

Variable Material Properties, Uniform Wall Heat Flux Boundary Conditions

These runs established the behavior of the simulations that form the basic results of this thesis. They incorporate the UDF code that introduces both the material properties tables and the uniform wall flux with unheated starting length. As hydrogen's thermophysical properties vary quite drastically with temperature (And pressure for density), the input mass flux and wall heat flux conditions had to be altered accordingly. This was done to maintain the previously specified exit velocity and wall temperature between all simulations conducted.

Variable Properties, Uniform Wall Heat Flux:

- Inlet:
  - $\mathrm{Re}_D = 80{,}139$
  - $\mathrm{T}_{Inlet} = 300\ \mathrm{K}$
  - $\dot{m} = 2.28\ \frac{gm}{s}$
- Outlet:
  - $\mathrm{Re}_D = 23{,}352$
  - $\mathrm{P}_{Outlet} = 3.06\ \mathrm{MPa}$
- Wall:
  - $q''_{Wall} = 3.5\ \frac{\mathrm{MW}}{\mathrm{m}^2}$
  - 5% unheated start

Variable Material Properties, Cosine Wall Heat Flux Boundary Conditions

For these runs the same UDF coding was used to produce a half-cosine wall-heat-flux profile in the axial direction as shown in **Equation 3.4 [2]**.

$$P(z) = \frac{\alpha P_{ave} L}{2\sin\left(\frac{\alpha L}{2}\right)} \cos\left[\alpha\left(\frac{L}{2} - z^*\right)\right] \qquad \textbf{Eq. (3.4)}$$

This profile is popular in the NTR community as a simple model to account for both the thermal energy generation and end losses in an NTR core **[2]**. P_{ave} scales the average flux along the tube length. The term α is a geometry scaling parameter. The values L and dimensionless z^* are used to scale the profiles to the 95% of the tube length that is heated. The UDF code sets heat flux to zero for the unheated starting length.

Variable Properties, Cosine Wall Profile Heat Flux:

- Inlet:
    - $\mathrm{Re}_D = 74{,}162$
    - $\mathrm{T}_{Inlet} = 300\ \mathrm{K}$
    - $\dot{m} = 2.11\ \frac{gm}{s}$
- Outlet:
    - $\mathrm{Re}_D = 18{,}515$
    - $\mathrm{P}_{Outlet} = 3.06\ \mathrm{MPa}$
- Wall:
    - $P_{ave} = 3.75\ \frac{\mathrm{MW}}{\mathrm{m}^2}$
    - 5% unheated start

Governing Equations

ANSYS-Fluent is a finite-volume Navier-Stokes solver that incorporates a Reynolds-averaged or eddy viscosity turbulence model. There are several built-in eddy viscosity models available. After reviewing the literature and performing preliminary simulations of constant-heat-flux tube flow heat transfer, the *k-ω* SST (Shear Stress Transport) 2-equation eddy-viscosity turbulence model with an additional intermittency function was selected. The NTREES system has a relatively short flow length measured in numbers of tube diameters, and the *k-ω* SST model appears to perform well in the developing regions of the tube. This point will be discussed in more detail in Chapter 4 when the simulation results are presented.

The governing equations are presented here in Cartesian form as that is how the model geometry was constructed. This was done with the anticipation of future simulation runs being scaled up to multiple cooling channels and a solid Tungsten domain included in the model.

Mass Conservation, Navier-Stokes and Energy Equations:

The equation set solved by ANSYS-Fluent is the mass conservation equation **(3.5)**, momentum equation **(3.6)** with the Newtonian stress tensor **(3.7)**, and the energy equation **(3. 8).** The effective thermal conductivity and the energy terms considered in **Equation 3.8** are defined by **Equation 3.9 [44]**. The equations are presented in conservative form. ANSYS-Fluent solves these equations with variable properties included in the gradients as shown.

$$\frac{\partial \rho}{\partial t} = -\nabla \cdot (\rho \vec{v}) \qquad \textbf{Eq. (3.5)}$$

$$\frac{\partial}{\partial t}(\rho \vec{v}) = -\nabla \cdot (\rho \vec{v}\vec{v}) - \nabla \mathrm{P} + \nabla \cdot (\bar{\bar{\tau}}) + \rho \vec{g} + \vec{F} \qquad \textbf{Eq. (3.6)}$$

$$\bar{\bar{\tau}} = \mu\left[(\nabla \vec{v} + \nabla \vec{v}^{T}) - \frac{2}{3}\nabla \cdot \vec{v} I\right] \qquad \textbf{Eq. (3.7)}$$

$$\frac{\partial}{\partial t}(\rho E) = -\nabla\cdot\left(\vec{v}(\rho E + \rho)\right) + \nabla\cdot\left(k_{eff}\nabla \mathrm{T} - \sum_j h_j\vec{J}_j + (\bar{\bar{\tau}}\cdot\vec{v})\right) + S_h \qquad \textbf{Eq. (3.8)}$$

$$k_{eff} \equiv k + k_t,\ E \equiv h - \frac{P}{\rho} + \frac{v^2}{2} \qquad \textbf{Eq. (3.9)}$$

The gravitational and general body force terms in **Equation 3.6**, $\rho\vec{g} + \vec{F}$, are set to zero. The term in **Equation 3.8**, $\sum_j h_j\vec{J}_j$, is the species diffusion term which is zero for this single species, single phase flow. The last term, S_h, is an internal energy source term which is zero, however viscous dissipation was operating for this study.

k-ω SST (Shear Stress Transport) Viscosity Model Equations:

Turbulent Kinetic Energy & Specific Dissipation Rate Transport Equations:

The equation for modeling the transport of turbulent kinetic energy (*k*) is provided as **Equation 3.10**. The equation for modeling the transport of specific rate of dissipation of turbulent kinetic energy (Turbulence frequency, *ω*) is provided as **Equation 3.11**. For both **Equation 3.10** and **Equation 3.11**, the same structure is present. The LHS term is set to zero as the flow is assumed steady state. The first term in the RHS represents the flux of the quantities *k* and *ω*. The terms Γ_k and Γ_ω, seen in **Equation 3.12**, are the effective diffusivity of their associated quantities. G_k and G_ω are the generation terms for *k* and *ω*. Y_k and Y_ω are the dissipation terms for *k* and *ω*.

The value D_ω is for flow cross-diffusion while S_k and S_ω represent source scalar terms manually input by a user. For this study, all source terms are set to zero **[44]**. It is important to note that all original constants developed by Menter **[48]** were maintained and unaltered during this study.

$$\frac{\partial}{\partial t}(\rho k) = -\frac{\partial}{\partial x_i}(\rho k u_i) + \frac{\partial}{\partial x_j}\left(\Gamma_k \frac{\partial k}{\partial x_j}\right) + G_k - Y_k + S_k \qquad \textbf{Eq. (3.10)}$$

$$\frac{\partial}{\partial t}(\rho \omega) = -\frac{\partial}{\partial x_i}(\rho \omega u_i) + \frac{\partial}{\partial x_j}\left(\Gamma_\omega \frac{\partial \omega}{\partial x_j}\right) + G_\omega - Y_\omega + D_\omega + S_\omega \qquad \textbf{Eq. (3.11)}$$

$$\Gamma_k = \mu + \frac{\mu_t}{\sigma_k},\ \Gamma_\omega = \mu + \frac{\mu_t}{\sigma_\omega} \qquad \textbf{Eq. (3.12)}$$

Numerical Domain, Meshing and Validation

Mesh Sizing Considerations

With any CFD simulation study, the mesh placed over the defined numerical domain is of great importance as it directly influences the solution and convergence characteristics. As this simulation study was set up to use the *k-ω* SST (Shear Stress Transport) equation model, it was known that the mesh first cell center had to be sufficiently small such that the first cell off the wall has a y^+ value than 1. Also, it is important that the mesh growth rate in the direction normal to the tube wall be very near or less than 1.1. The mesh growth rate is measured as the increase in a mesh element's edge length in a specified direction for each successive mesh layer. This means that for a mesh growth rate of 1.1, the mesh element's edge length will be 110% of the length of the element before it in the normal direction to the wall **[44]**. During preliminary mesh evaluation and testing, the model was shown to have a high level of sensitivity to large mesh growth rates (> 1.25). For that reason, care was taken to insure mesh growth rates very near 1.1. As the final mesh was used for both the constant and variable properties simulation runs, the value of one y^+ unit was selected to be sufficient for the constant properties runs and more than sufficient for the variable-property run. The resulting first cell off the wall cell-center y^+ values of simulations run for this study can be seen in **Table 4-1**.

For ease of manipulating the mesh within ANSYS' mesher GUI, the single tube geometric domain was split into five different fluid domains. Four circumferential domains and one center domain (see **Figures 3.11** and **3.12**). This allowed much more control of the near wall element sizing while maintaining the element growth rate normal to the wall. A simple summation calculator was created in Excel to best select the number of divisions and bias factor in the radial direction for the outside fluid domains. The bias factor is the last cell edge length divided by the first cell normal to the wall's edge length. Hence a bias factor of 50 means the last cell in line normal to the wall has an edge length 50 times that of the first cell. The ratio between the number of edge divisions and bias factor for said edge were used as a means to control cell growth rate and keep it within acceptable values required for the k-ω SST model.

Four meshes were used in the validation process. First, mesh A consists of 546,000 elements. The mesh A radial edge sizing parameters were set to 15 radial divisions, a bias factor of 10 and 5 circumferential divisions for each outer fluid domain (20 total circumferentially) with 1500 streamwise divisions. The mesh settings for radial edge sizing can be found in **Table 3-1**, while a general view of mesh A's 5-fluid domains can be seen in **Figure 3.11**.

Table 3-1: Mesh Sizing Overview

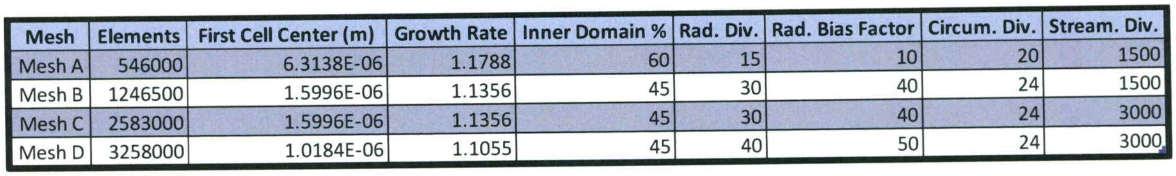

Mesh	Elements	First Cell Center (m)	Growth Rate	Inner Domain %	Rad. Div.	Rad. Bias Factor	Circum. Div.	Stream. Div.
Mesh A	546000	6.3138E-06	1.1788	60	15	10	20	1500
Mesh B	1246500	1.5996E-06	1.1356	45	30	40	24	1500
Mesh C	2583000	1.5996E-06	1.1356	45	30	40	24	3000
Mesh D	3258000	1.0184E-06	1.1055	45	40	50	24	3000

Second, meshes B and C have radial edge sizing settings of 30 divisions and a bias factor of 40. They have 24 total circumferential divisions (compared to 20 in mesh A). The fluid domain geometry was also changed such that the inner domain was 45% the total channel radius (compared to 60% in mesh A). This was done to reduce adjacent cell size difference between the inner most cell of the four outer domains and the outer most cells of the center fluid domain, as well as keeping the cell normal to wall expansion rate in check (See **Figure 3.12**). Mesh B was made up of 1500 streamwise divisions, while mesh C has 3000 streamwise divisions. Otherwise, meshes B and C are comprised of the same radial settings. The mesh settings for radial edge sizing can be found in **Table 3-1**. Also see **Table 3-1** and **Table 4-1** for the total element count, first-cell center height, first-cell y^+ value, and various sizing parameters for each mesh.

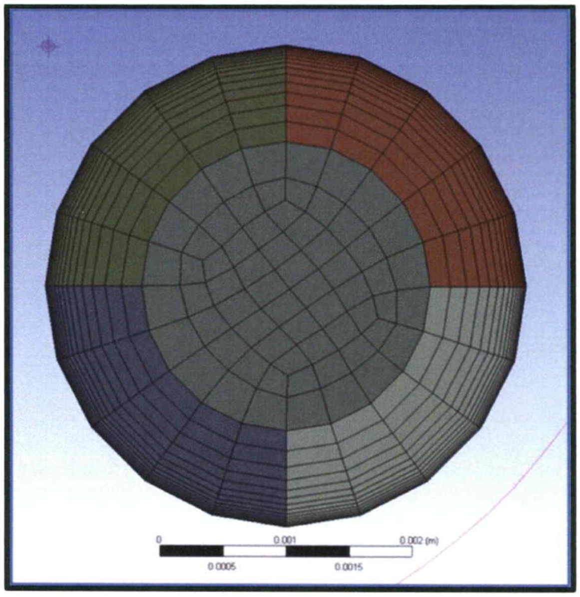

Figure 3.11: Mesh A General View

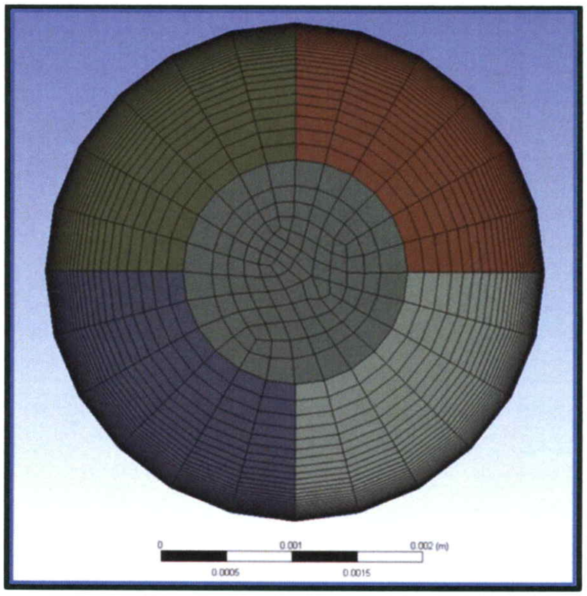

Figure 3.12: Meshes B and C General View

NOTE: Meshes B and C Inner domain radius is 45% of the total radius and has 24 circumference divisions (Mesh A's inner radius is 60% with 20 circumferential divisions).

Finally, mesh D, seen in **Figure 3.13**, was used as a final validation for the constant properties, uniform, flux simulation runs, as these runs had the largest first-cell y^+ values when compared to the variable-property simulations. Mesh D has radial edge sizing settings of 40 divisions and a bias factor of 60. It, like meshes B and C, has 24 total circumferential divisions and the fluid inner domain geometry was 45% the total channel radius. Like mesh C, mesh D was made up of 3000 streamwise divisions. Again, mesh D was only run for constant properties, uniform flux runs to insure meshes B and C had a sufficient radial sizing configuration and the solutions were not changing with added cell layers normal to the tube wall. This was due to meshes A, B and C having first-cell values of $y^+ > 1$ for constant properties, uniform flux runs.

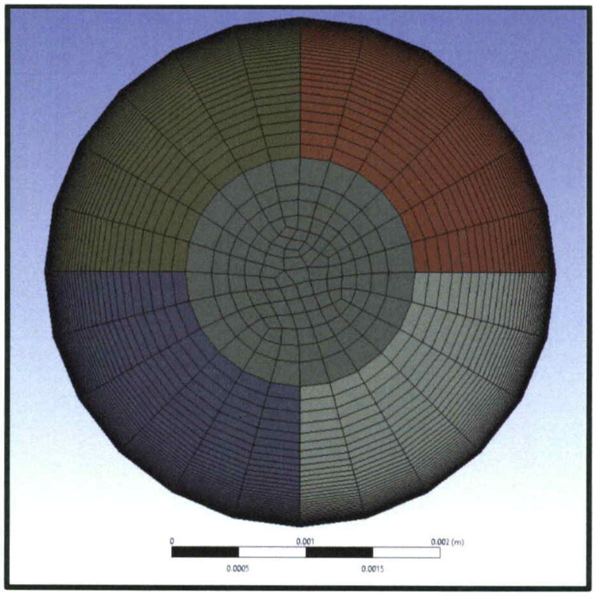

Figure 3.13: Mesh D General View

Mesh Validation

Meshes A, B and C were run for all three boundary conditions. All showed monotonic convergence to a single solution with increasing mesh resolution. An additional run with mesh D was conducted for the case of constant fluid properties and uniform wall heat flux. Mesh D incorporated the refinements explained in the previous subsection. Mesh D maintains a first-cell $y^+ < 1$ for the uniform-flux boundary condition while exhibiting equivalent solution profiles as meshes B and C. Once the solution profiles ceased to change with increasing mesh resolution, the coarsest mesh <u>at the final solution profile</u> was selected as the primary mesh for all further simulation runs for this study. In this case, mesh B showed results that represented the converged evolutions of Nusselt number while maintaining shorter simulation times. Graphs from the mesh validation runs will be discussed with the other results in Chapter 4.

CEL Code Development and Data Exporting

After simulations have converged to a solution, data much be exported and processing to obtain the values of interest listed previously in Chapter 3. The ANSYS-CFD-Post processor, provide by ANSYS, was used for data exporting. The exporting of common parameters at a wall, an iso-line, plane or individual node was as easy as selecting the desired values in CFD-post's software GUI and exporting to the designated location. It is important to mention that the default settings of ANSYS-CFD-Post export data at mesh <u>nodes</u>, not at <u>cell center</u> or <u>volume centers</u>. This is an extremely important point to consider especially when reviewing near-wall solutions corresponding to a cell-centered y^+ value as a means to size meshes.

For more specific parameters such as the bulk temperature and other bulk properties that were used extensively in this study (as the "bulk" fluid was a primary reference frame used), custom CFX Expression Language (CEL) code Session files had to be written to add to ANSYS-CFD-post's state file. The bulk values were obtained by **Equation 3.1** substituting in the various variables required as φ. The equation is a summation of data in the x-y plane at a given streamwise z-location of the flow. For simplicity, 100 equally spaced plane locations were created (ranging from $0 < \frac{Z}{L} < 99$) via the CEL code and made to be easily adapted to different physical geometries and more resolution for future model scale ups. Additionally, 15 more streamwise planes were created to be locations for radial data exporting. Ten of the radial data planes were created and spaced closely within the developing flow region as it was a key location for investigation in this study. The additional five planes equally spanned the rest of the z-direction giving a complete overview of the model's radial characteristics from tube entrance to exit.

After the planes were created, CFD-post requires expressions to be written designating an equation or process to be performed on specific data ANSYS-Fluent exports to ANSYS-CFD-Post for further processing (Users can specify which values are required in a simulation for Fluent to export to CFD-Post to save files space). Then, variables were created based on said expressions at specified plane locations. As each bulk value at the z-plane locations yield single numerical values, each required a designated CEL variable name. Each name denoted the flow value in question and plane location which data was pulled from for computing. Variables were made for bulk fluid: Temperature, Density, Dynamic Viscosity, Constant Pressure Specific Heat, Thermal Conductivity, and Velocity. In total 630 custom bulk variables for streamwise analysis, plus an additional 90 bulk variables to compliment radial analyses were created. Once the session files, made via CEL code were ran, the ANSYS-CFD-post software integrated the planes, expressions and variables into the current master-state file. At this point, users can export all future simulation data completely from the ANSYS-CFD-Post GUI to files for further processing and analysis.

A note to future users of the post-processor: Session files must be run via ANSYS-CFD-Post opened from the file explorer bin NOT ANSYS Workbench. After the Session files have been run and saved to the master-state file, it does not matter how the user opens ANSYS-CFD-Post for future processing and data exporting. After data files for wall and bulk values at both streamwise (z-direction) and radial (x-y iso-lines at given z-positions) were created, the values were copied over into "streamwise" and "radial" specific Excel workbooks to obtain various dimensionless parameters, profiles, graphs and other calculations.

CHAPTER 4

CFD Simulation Results

Validation Study for the Case of Constant Material Properties, Uniform Heat Flux

The first stage in the investigation was to qualify the model build by simulating a uniform property flow with a uniform-heat-flux boundary condition. The parameter values are given in Chapter 3 along with a discussion of these choices. The simulation was run with meshes A, B, C and D and the *k*-*ω* SST model. The streamwise evolution of centerline velocity profile, **Figure 4.1**, produces the velocity increase above the developed centerline value as seen in past works by Duz **[31]** and Doherty **[32]** reviewed in Chapter 2. As the boundary layer thickens, the momentum of the fluid near the tube wall decreases and the centerline flow must accelerate to maintain continuity. The centerline velocity maximum occurs at the streamwise position where the pipe boundary layers merge **[31]**. Shortly downstream, the centerline velocity decreases to a uniform plateau. At this point, the flow has reached its hydraulic development length.

As the Prandtl number for this study is that of a gas ($Pr = 0.68$), it is expected that the thermal development length will be accomplished as soon as the hydraulic development length is reached. This is the case here as shown in **Figure 4.1** for the streamwise evolution of centerline velocity, and in **Figure 4.2** for the streamwise evolution of Nusselt number. The 5% unheated starting length does not significantly affect this outcome. The streamwise evolution of wall temperature and bulk fluid temperature is shown in **Figure 4.3**.

The results in **Figures 4.2** and **4.3** for all four meshes (A – D) converge to a single solution with increasing mesh density with meshes B, C, and D producing nearly identical solutions in these coordinates. The data in the developed region agrees with the Dittus-Boelter correlation for developed flow to a difference of less than 1%. The Gnielinski correlation is about 10.4% below the simulation results.

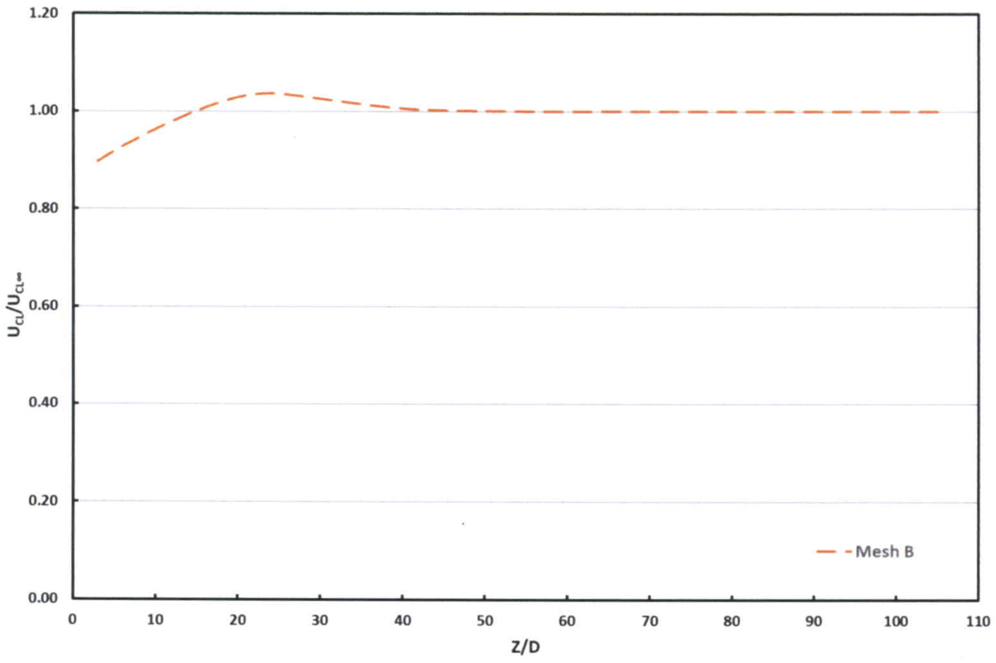

Figure 4.1: Constant Properties, Uniform Flux Validation Centerline Velocity Profile, Run 6

A small dip in Nusselt number and a corresponding small overshoot in wall temperature can be seen in the developing region in **Figures 4.2** and **4.3**, respectively. In the developing region, Nu_b rapidly drops to a minimum of $Nu_b = 152$ in response to the boundary layer growing and thus, insulating the flow of heat from the wall to bulk fluid of the tube. This is an expected phenomenon for the developing region in a flow such as this. Then, Nu_b increases to a plateau value of $Nu_b = 155$, a 2% rise. The overshoot in wall temperature in **Figure 4.3** is barely discernable in the figure. Note that the bulk fluid temperature increases linearly as expected for this boundary condition.

Figure 4.4 shows the evolution in skin friction coefficient, defined by **Equation 4.1**, and there is again a dip of about 4% relative to the plateau value in the developing region. **Equations 4.2** through **4.4** are popular correlations for fully developed turbulent tube flow. **Equation 4.2** is suggested for $1 \times 10^4 \leq Re_D \leq 5 \times 10^4$ **[49]**. As the constant properties, uniform wall heat flux case was run at 75,000, the *Karman-Nikuradse* ***E*****quation 4.3** was also included. The *Karman-Nikuradse* equation is stated to produce best results for $3 \times 10^4 \leq Re_D \leq 1 \times 10^6$ **[49].** Last is **Equation 4. 4** for $1 \times 10^4 \leq Re_D \leq 5 \times 10^6$, proposed by Petukhov **[49]**. The developed region agrees well with the correlations with a difference in the fully developed flow region of about 1.8% with **Equation 4.2**.

$$C_f \equiv \frac{\tau_w}{\frac{1}{2}\rho V^2}$$ **Eq. (4.1)**

$$\frac{C_f}{2} = 0.039 Re_D{}^{-0.25}$$ **Eq. (4.2)**

$$\frac{C_f}{2} = 0.023 Re_D{}^{-0.2}$$ **Eq. (4. 3)**

$$\frac{C_f}{2} = (2.236 \ln Re_D - 4.639)^{-2}$$ **Eq. (4.4)**

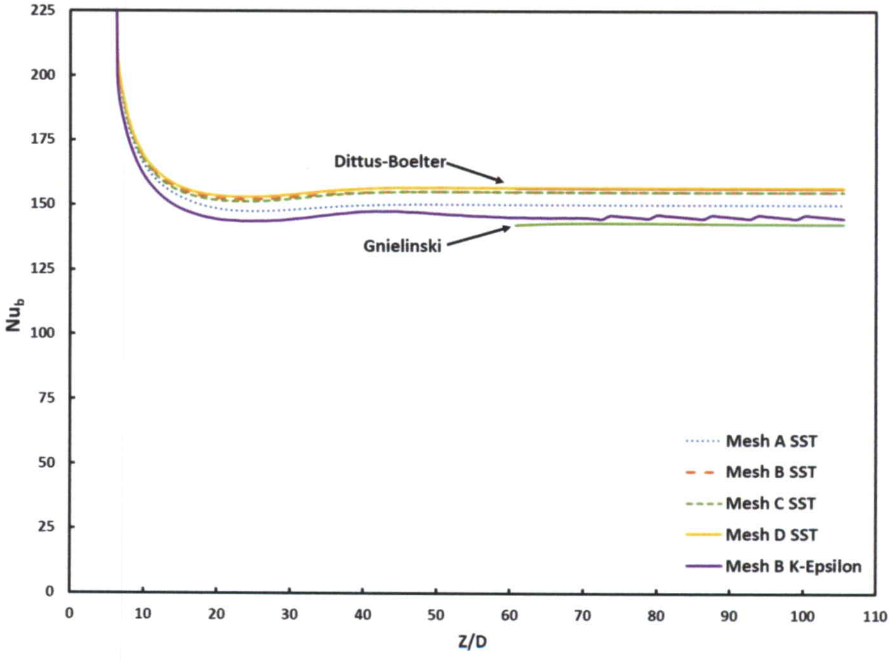

Figure 4.2: Constant Properties, Uniform Flux Axial Nu_b Profiles

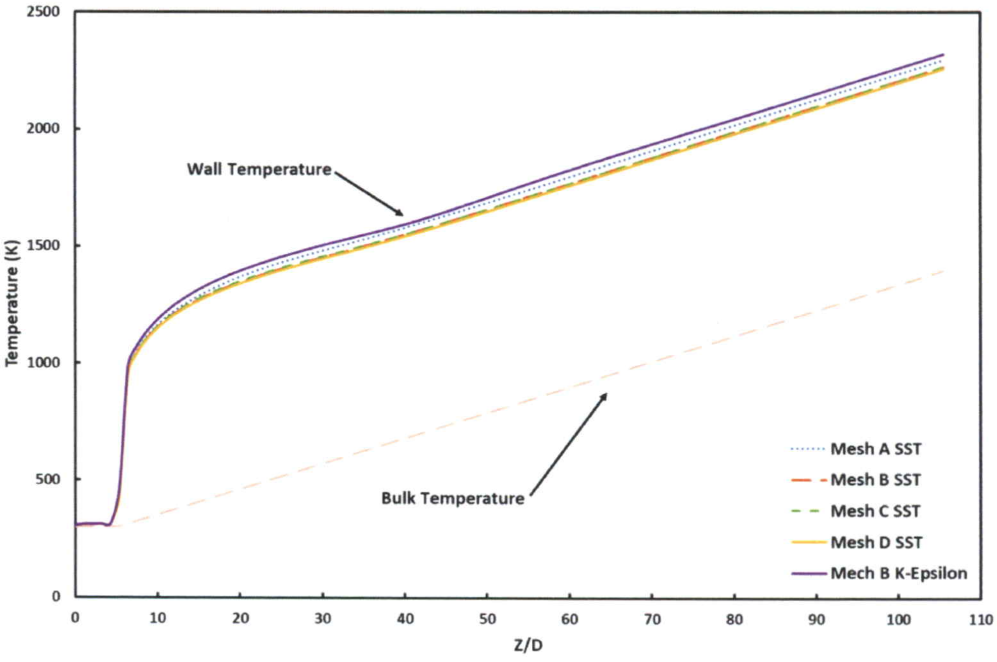

Figure 4.3: Constant Properties, Uniform Flux Axial Temperature Profiles

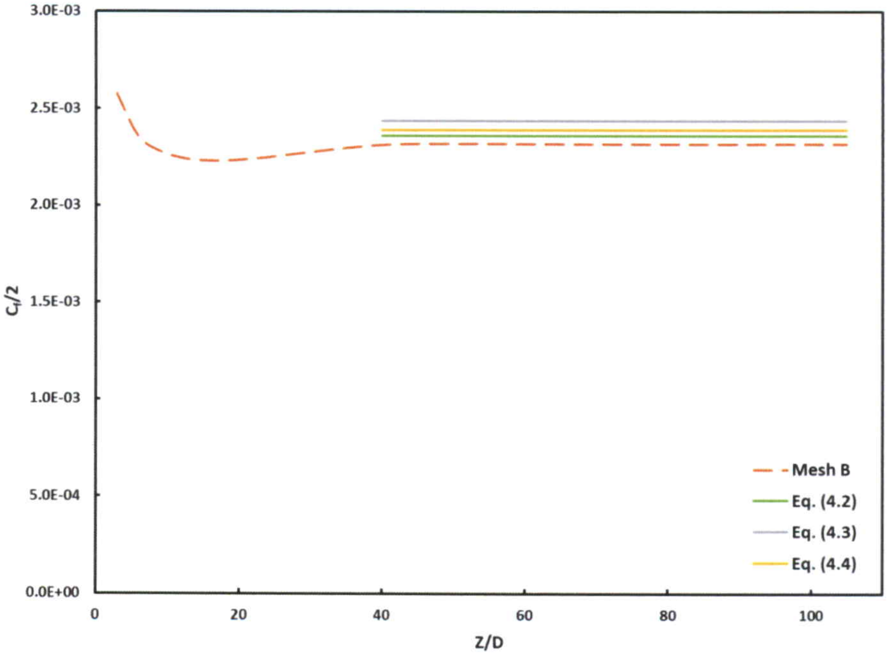

Figure 4.4: Constant Properties, Uniform Flux Axial Skin Friction Coefficient Profile, Run 6

The departure from monotonic behavior in Nu_b, wall temperature, and skin friction in the developing and transitioning region of the tube is not a feature of classical solutions as represented in popular convection texts. Canonical closed-form solutions generally assume a thermal layer developing into a fully developed momentum profile and do not show the non-monotonic behavior. Co-developing layers in turbulent tube flow are usually represented in texts by graphs sourced from experimental data, and these experiments may have missed this issue. On first encounter, this research group assumed the issue to be an artifact of RANS modeling in general or the k-ω SST turbulence model in particular. To address the latter concern, the simulation was executed with a k-ε turbulence model and the behavior remained present. The solution produced via the k-ε model, as seen in **Figures 4.2** and **4.3**, was shown to have a more drastic non-monotonic behavior for axial temperature and Nusselt number profiles. Consider the Nusselt number axial plot (**Figure 4.2**), the profile exhibited a "searching" phenomenon where the values drop, rebound and then drop again to a fully developed solution. The solution yielded results similar to the k-ω SST solution run with mesh A, the coarsest near-wall mesh considered. In addition, the k-ε model produced a saw-toothed evolution in Nu_b for $(\frac{Z}{D}) > 70$ (again, see **Figure 4.2**).

The literature reviewed in Chapter 2 offers support for the non-monotonic behavior of *Nu* in the developing region of the flow. These studies include both experimental work by Deissler **[29]** and analytical treatments such as those by Chen **[28]** and **Malik [33]**. We conclude that while this behavior was unexpected, it is not without support. It may be that the *k-ω* SST turbulence model is capturing a representation of the interplay between the growth of the thermal layer and the maturation of the turbulence structure in the co-developing viscous layer.

This will become important in the remainder of the study as the non-monotonic behavior will become strongly magnified in the presence of high levels of wall heat flux and fully variable material properties.

Radial profiles of streamwise velocity and temperature were evaluated as part of the validation of the constant-properties, uniform flux model. The values for dimensionless velocity (U^+) and dimensionless distance normal to the tube wall (y^+) are defined in **Equation 4.5**. The axial location $(\frac{Z}{D}) = 79$ was selected as it is well into the fully developed region. **Equations 4.6** and **4.7** give the standard wall model for dimensionless velocity (U^+) as a function of dimensionless distance normal to the tube wall (y^+) **[50]**. **Figure 4.5** shows the expected agreement with the wall model for meshes B and D. Note the slightly positive wake.

$$U^+ \equiv \frac{U}{u_\tau},\ y^+ \equiv \frac{yu_\tau}{\nu},$$

Eq. (4.5)

Where: $u_\tau \equiv \sqrt{\frac{\tau_w}{\rho}}$ and $\tau_w \equiv \mu\left(\frac{\partial u}{\partial y}\right)|_{y=0}$

for: $y^+ < 5$,

Eq. (4.6)

$$U^+ = y^+$$

for: $y^+ > 30$,

$$U^+ = \kappa \ln y^+ + C;$$ **Eq. (4.7)**

$$\kappa = 0.41,\ B = 5.2$$

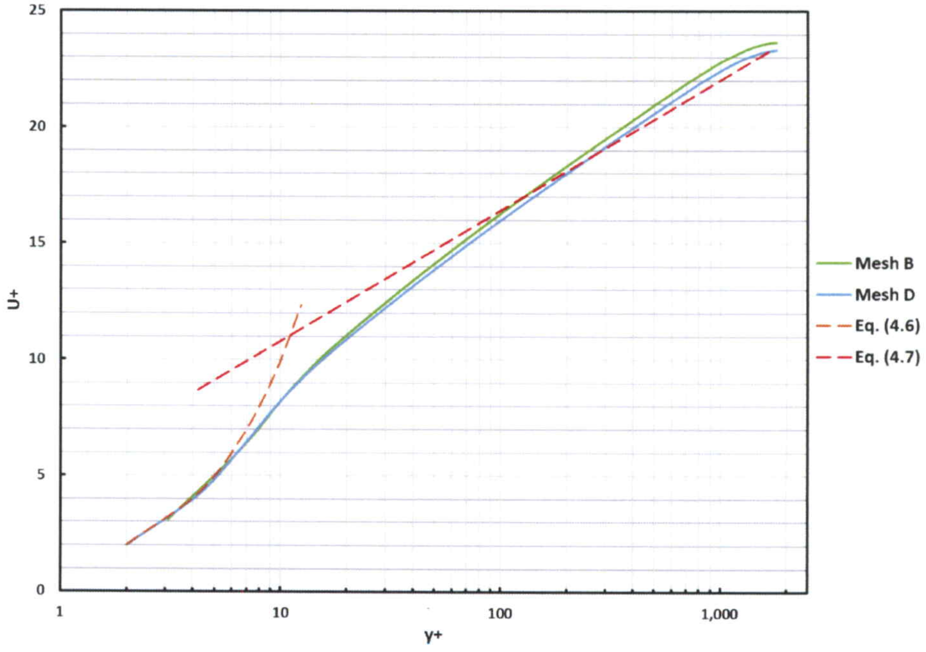

Figure 4.5: Constant Properties, Uniform Flux $log(y^+)$ *vs.* U^+ *at* $(\frac{z}{D}) = 79$

The dimensionless temperature (T^+) is defined in **Equation 4.8**. The thermal wall model is given in **Equation 4.9 and 4.10 [49]**. The plot for dimensionless temperature (T^+) verses dimensionless wall distance (y^+) can be seen in **Figure 4.6**. Note that results for the two meshes shown coincide. Data in the log-law region are slightly lower than **Equation 4.10**. The profile was further investigated and compared to the results of Deissler discussed in Chapter 2 **[30]**. **Figure 4.7** from Deissler's TN-3145 shows a plot of T^+ versus y^+ at various Prandtl numbers. The present data for $Pr = 0.68$ lie just below Deissler's curve for $Pr = 0.73$. This concludes the presentation of the constant-properties, uniform flux validation run.

$$T^+ \equiv \frac{\theta}{St_\tau},$$

Eq. (4.8)

Where: $\theta \equiv \frac{T-T_w}{T_b-T_w}$ and $St_\tau \equiv \frac{h}{\rho C_p u_\tau}$

for: $y^+ < 5$,

Eq. (4.9)

$$T^+ = y^+ Pr$$

for: $y^+ > 30$,

Eq. (4.10)

$$T^+ = 2.2 \ln y^+ + 13.39 Pr^{2/3} - 5.66$$

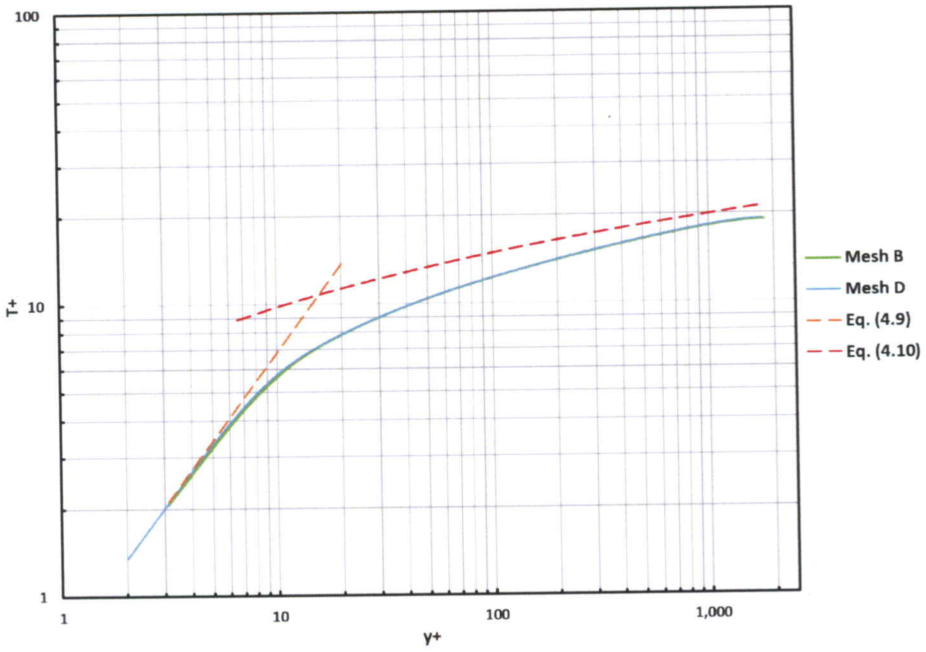

Figure 4.6: Constant Properties, Uniform Flux T^+ *vs* y^+ *at* $(\frac{z}{D}) = 79$*,* $Pr = 0.68$

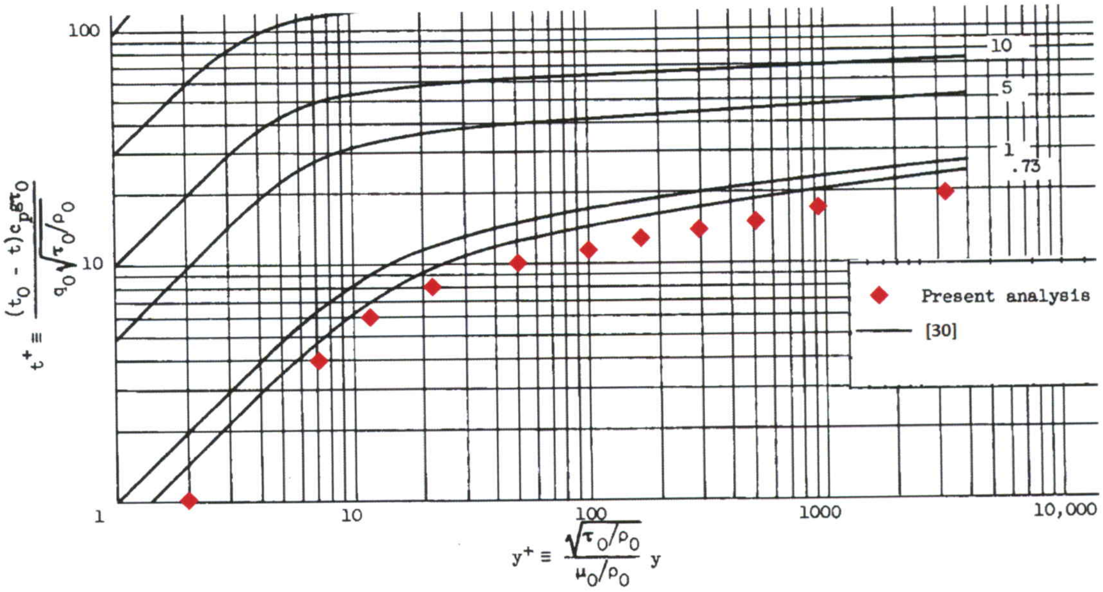

Figure 4.7: T^+ *vs.* y^+ *for Various Prandtl Numbers* ***[30, Fig. 2].***
Present Analysis Included for Comparison: $(\frac{z}{D}) = 79$*,* $Pr = 0.68$

Results for the Case of Variable Material Properties, Uniform Heat Flux

Table 3-1 and **Table 4-1** provide a summary of the simulation runs and associated meshes used in this study. The y^+ values quoted are for the first cell center off the wall. Both values averaged over the full duct length and values for the average after $(\frac{Z}{D}) > 60$ downstream (fully developed region) are given. As seen in the tables, mesh D was run for only the constant material properties, uniform-wall-flux validation run. This was done to investigate concerns that the size of the entry region first-cell y^+ values was the cause for the dip in the Nusselt number values in the developing region. As it is known that the k-ω SST turbulence model requires a mesh sufficiently small such that the first cell center $y^+ < 1$. Mesh D fell very nicely in line with meshes B and C for the key values of interest such as axial temperature profiles. These results showed no obvious solution changes with the increased mesh resolution. This outcome gave the confidence needed to move forward with mesh B as the primary simulation mesh. Mesh B has fast convergence times while maintaining a high level of accuracy when compared to finer resolution meshes in both the streamwise and radial direction flow profiles.

Table 4-1: Primary Simulation Runs Overview and Cell Center y^+ Values

Run #	Run Name	Heat Flux (MW/m2)	Mass Flux (kg/m2/s)	Ω (kJ/kg)	(Z/D)	Total Avg Y^+	Z/D > 60 Y^+	ReD Inlet	ReD Outlet
1	Mesh_A_Const_Props_Const_Flux	17.0	425	17067	107	4.95	4.96	74727	74727
2	Mesh_B_Const_Props_Const_Flux	17.0	425	17067	107	1.54	1.55	74727	74727
3	Mesh_C_Const_Props_Const_Flux	17.0	425	17067	107	1.54	1.55	74727	74727
4	Mesh_D_Const_Props_Const_Flux	17.0	425	17067	107	0.96	1.00	74727	74727
5	Mesh_A_Vary_Props_Const_Flux	3.50	200	7467	107	2.25	2.02	80252	23307
6	Mesh_B_Vary_Props_Const_Flux	3.50	200	7467	107	0.55	0.51	80139	23352
7	Mesh_C_Vary_Props_Const_Flux	3.50	200	7467	107	0.55	0.51	80267	23360
8	Mesh_A_Vary_Props_Cosine_Flux	3.75	185	8649	107	2.58	1.63	74243	18478
9	Mesh_B_Vary_Props_Cosine_Flux	3.75	185	8649	107	0.67	0.42	74162	18515
10	Mesh_C_Vary_Props_Cosine_Flux	3.75	185	8649	107	0.67	0.42	74255	18517
11	Mesh_C_NTR_FULL_ROD	3.75	560	8436	315	-	-	162087	58640
12	Mesh_B_Vary_Props_Const_Ψ_2_75MWm2_Flux	2.75	157	7473	107	-	-	62973	18235
13	Mesh_B_Vary_Props_Const_Ψ_2MWm2_Flux	2.00	114	7485	107	-	-	45755	13179
14	Mesh_B_Vary_Props_Const_Ψ_1MWm2_Flux	1.00	57	7485	107	-	-	22887	6568
15	Mesh_B_Vary_Props_2_75MWm2_Flux	2.75	200	5885	107	-	-	80135	27081
16	Mesh_B_Vary_Props_2MWm2_Flux	2.00	200	4280	107	-	-	80131	31977
17	Mesh_B_Vary_Props_1MWm2_Flux	1.00	200	2140	107	-	-	80126	44675

The next step in the investigation was to see how the flow behaved when the hydrogen material properties could vary with the changes in temperature and pressure. The simulation was run against meshes A-C, but for clarity only the primary mesh B will be displayed in the results to come. The streamwise evolution in wall temperature, shown in **Figure 4.8**, exhibited a very rapid rise as soon as the wall heat flux was applied. Recall, the flow has a 5% unheated starting length. Variable properties responding to a wall heat flux of 3.5 MW/m^2 strongly exacerbated the small rise in wall temperature in the developing region seen in the constant-properties run in **Figure 4.3**. At $\left(\frac{Z}{D}\right) \approx 60$ downstream, the flow recovers toward the expected fully developed behavior for the uniform wall flux condition: the wall temperature more nearly parallels the bulk fluid temperature.

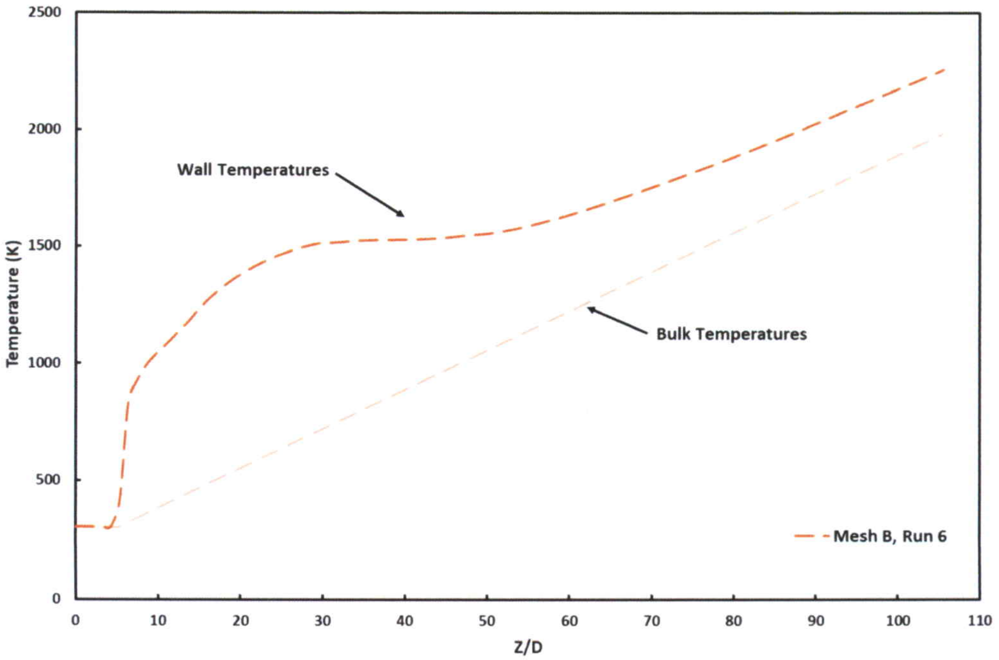

Figure 4.8: Variable Properties, Uniform Flux Axial Temperature Profiles

The corresponding evolution in Nusselt number is shown in **Figure 4.9**. Here the dip in Nu_b in the developing region is much more pronounced and the recovery to a fully developed value is less easy to identify and occurs as late as $\left(\frac{Z}{D}\right) \approx 80$ downstream. The reader should note two differences between this case and the preceding constant-properties case. The fully developed Nu_b is lower by more than half in the present case due to a reduced mass flux (see **Table 4-1**). The mass flux reduction was necessitated by the desire to meet the specified NTREES exit velocity and wall temperature (see Chapter 3) constraints while incorporating variable propellant properties. Second, the Reynolds number continues to decrease over the length of the tube in response to the changing dynamic viscosity under the constraint of fixed mass flux. This will be discussed in further detail in the pages to come. The far-downstream ($\frac{Z}{D} > 80$) behavior of Nu_b is in reasonable agreement with correlations shown from Dittus-Boelter and Gnielinski for canonical flows and in agreement with Taylor and Thomas for variable-property hydrogen flows. However, Taylor, Thomas, and Sieder-Tate do not fully capture the dip in Nu_b in developing region seen in the simulation results. Taylor and Thomas both show a small dip in about the correct location due to Reynolds number decreasing, but generally overpredict the value of Nu_b in the developing region.

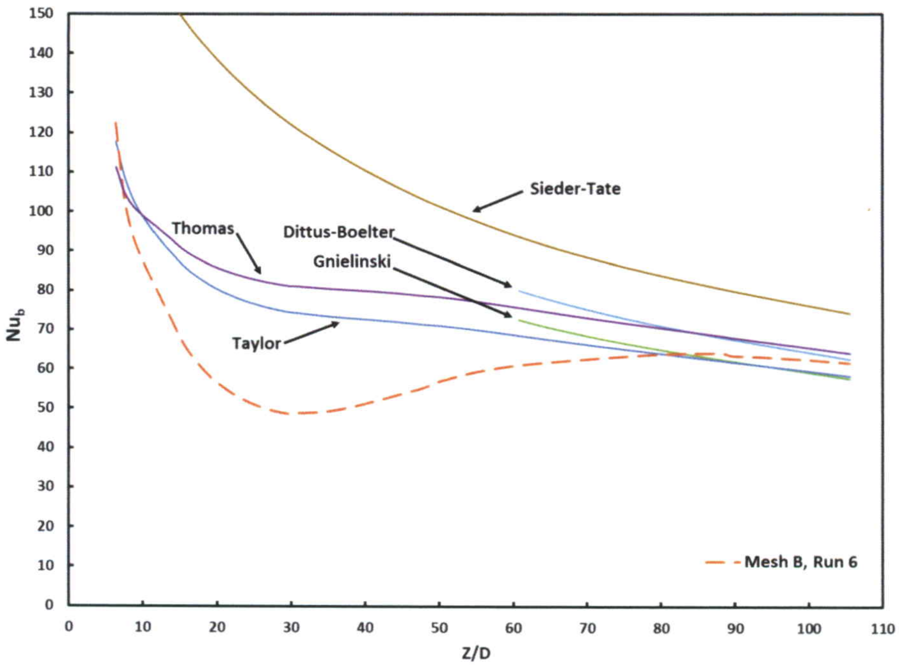

Figure 4.9: Variable Properties, Uniform Flux Axial Nu_b Profiles

Figures 4.10 and **4.11** show, respectively, radial profiles of streamwise velocity and dynamic viscosity. Regarding **Figure 4.10**, the first observation is the remarkable acceleration in the flow as internal energy is added to the fluid. The profiles are ordered from near-entrance in the lower portion of the graph to near-exit in the upper portion. The centerline values are nearly a factor of seven larger than the entrance values under the constraint of uniform mass flux. The velocity profiles in the developing region display a momentum excess relative to the centerline values approximately in the near-wall third of the profile. The dynamic viscosity, shown in **Figure 4.11** is relatively uniform in the downstream portion of the tube, but is strongly non-uniform (and higher near the wall) in the developing region of the tube.

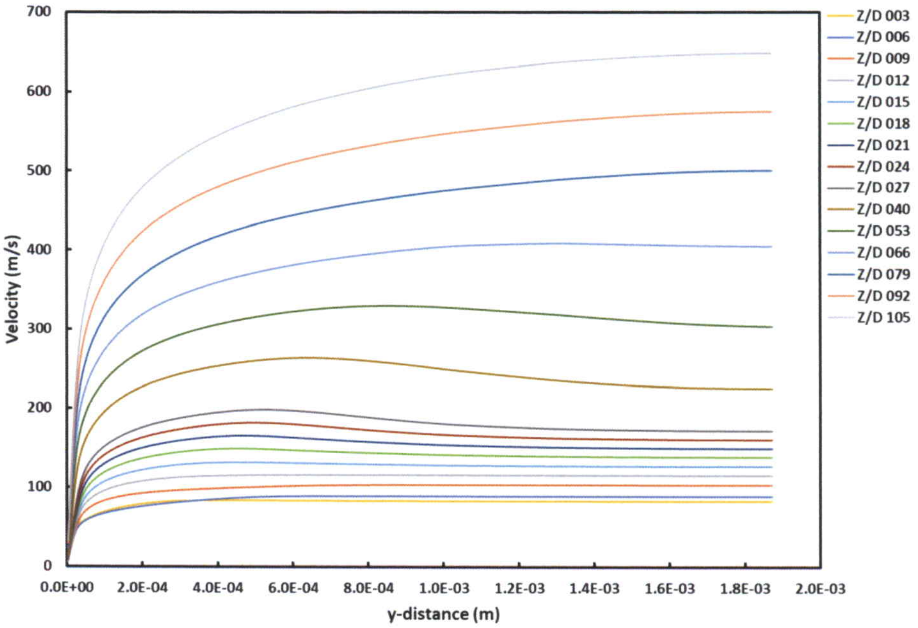

Figure 4.10: Variable Properties, Uniform Flux Radial Profile of Streamwise Velocity

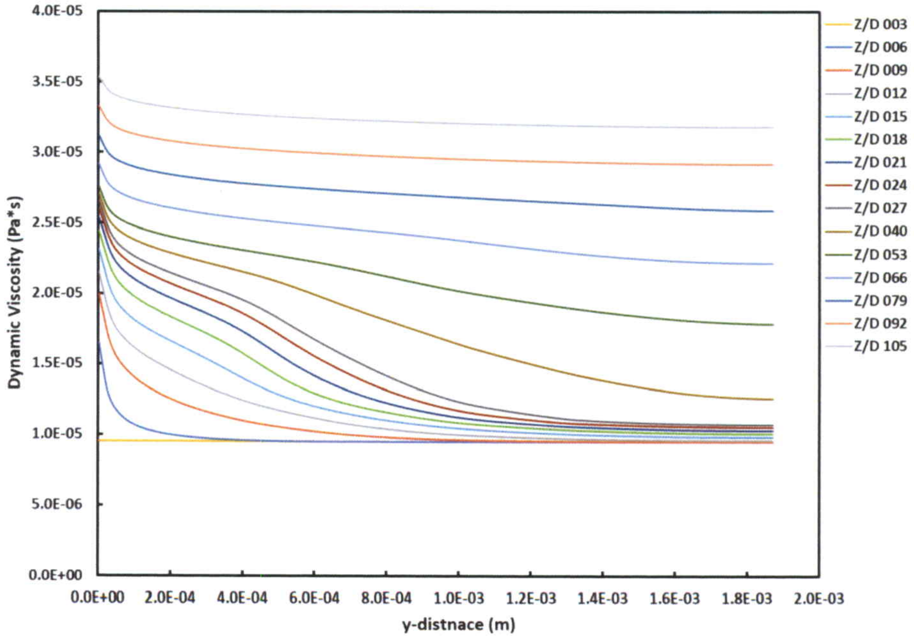

Figure 4.11: Variable Properties, Uniform Flux Radial Profile of Streamwise Dynamic Viscosity

The momentum excess observed in **Figure 4.10** is supported by the work of Youn and Mills **[22, Fig. 9]** and Chen (et. al.) **[28, Fig. 4]** (further discussed in Chapter 2). Both studies found a similar increased velocity approximately in the near-wall third of the profile relative to the centerline values. Youn and Mills provided radial graphs of the streamwise evolution of specific heat **[22, Fig. 8]** to be discussed as the potential causation for the non-monotonic developing region momentum and thermal radial profiles. However, the Youn and Mills flow was conducted at cryogenic temperatures very near the critical temperature for hydrogen (33.145 K). This caused the flow to exhibit much more abrupt material property changes that are not present to the same degree of severity as the current study. They attributed the presence of the velocity profile "overshoot" to the behavior of specific heat at or near the critical point or a "pseudo-critical" point creating a "thermal spike" phenomenon. Youn and Mills describe a "pseudo-critical temperature", one in which occurs above the critical pressure for hydrogen, but still produces a "thermal spike" due to a spike in the specific heat profile at a given temperature. The study states the presences of a "thermal spike" far above the critical pressure was observed for flows with high heat flux and low mass flow rate.

Chen (et. al.) concluded that a non-parabolic radial profile is present for both the evolution of mean streamwise velocity **[28, Fig. 4]** and temperature **[28, Fig. 8]**. These non-parabolic resulting profiles are shown to be more drastic in the developing region of the parallel channel flow. The local maxima for velocity in the developing region was shown to again be not at the centerline, but approximately in the near-wall third of the profile relative to the centerline values. This is in agreement with the current study.

The current study exhibits no spike in specific heat at the temperatures simulated (see **Figure 3.7**), however it does produce a similar "thermal spike" phenomenon and sensitivity to high wall heat flux as discussed by Youn and Mills. Shown in **Figure 4.12** are radial plots for the streamwise evolution of the difference between wall and local temperature ($T_W - T$) versus the radial distance from the wall, ($\frac{y}{R} = 1$ being the flow centerline). The ΔT is shown to grow to a maximum exceeding 1100 K at $\left(\frac{z}{D}\right) = 27$ before subsiding as the flow becomes fully developed. This trends well with Chen (et. al.) **[28, Fig. 8]**.

Both the work of Youn and Mills and by Chen (et. al.) seem to display a sensitivity to Reynolds number. That being a higher inlet Reynolds number dampens the observed non-monotonic profiles in the developing regions of the flow. This observation will be further discussed in Chapter 6 for future work.

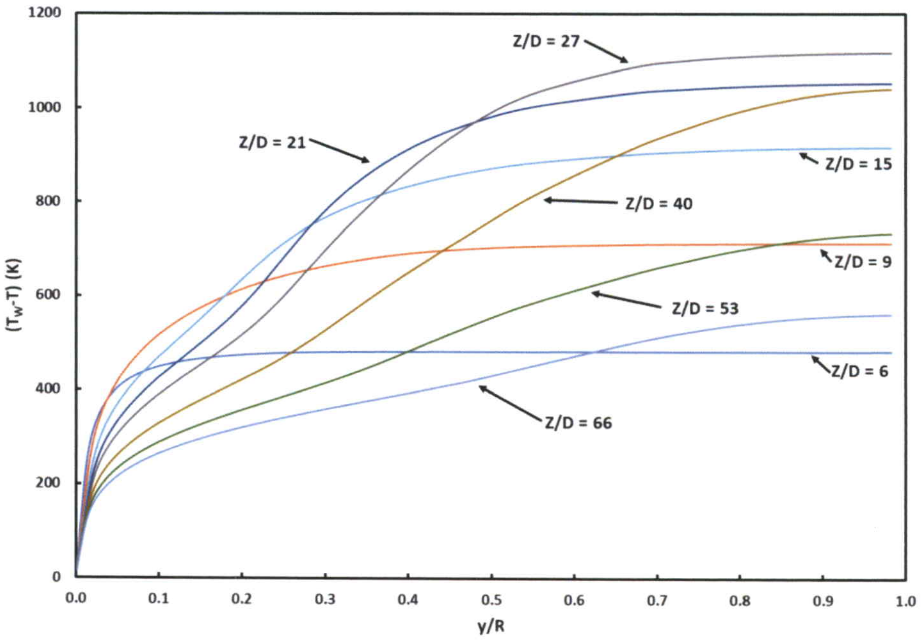

Figure 4.12: Variable Properties, Uniform Flux Radial Profile of Streamwise Temperature

Results for Runs with Variable Material Properties, Uniform Heat Flux

Once the non-parabolic radial profiles and thus, non-monotonic axial profiles were observed and supported by past literature, the study investigated the sensitivity of the non-monotonic development region phenomena further. To allow various (uniform) wall flux levels to be compared with a physically meaningful scaling present, a scaling parameter must be created. A ratio describing the total wall heat transfer rate over the tube length delivered per unit mass flux (kJ/kg) is given in **Equation 4.11**. Let us refer to this value as Ψ within this document for simplicity.

$$\Psi = \frac{Energy\ Addition\ (L)}{Mass\ Flow} = \frac{4q''\left(\frac{Z}{D}\right)}{\dot{m}''} \qquad \textbf{Eq. (4.11)}$$

This ratio was a means to throttle heat flux and mass flux while maintaining the same bulk and maximum exit wall temperature for variable material properties, uniform wall heat flux flow cases. Four runs with different combinations of boundary conditions were selected, all while holding Ψ constant at ~ 7470 kJ/kg (See **Table 4-1**). The intent of these four runs was to compare the degree of non-monotonic behavior exhibited under the constraint of constant heat addition per unit mass flux in the developing region where the fluid is transitioning to turbulence and being exposed to high levels of heat flux. The results for wall and bulk temperature are shown in **Figure 4.13.** The associated axial evolution in Reynolds number and in bulk axial velocity are shown in **Figures 4.4** and **4.5**.

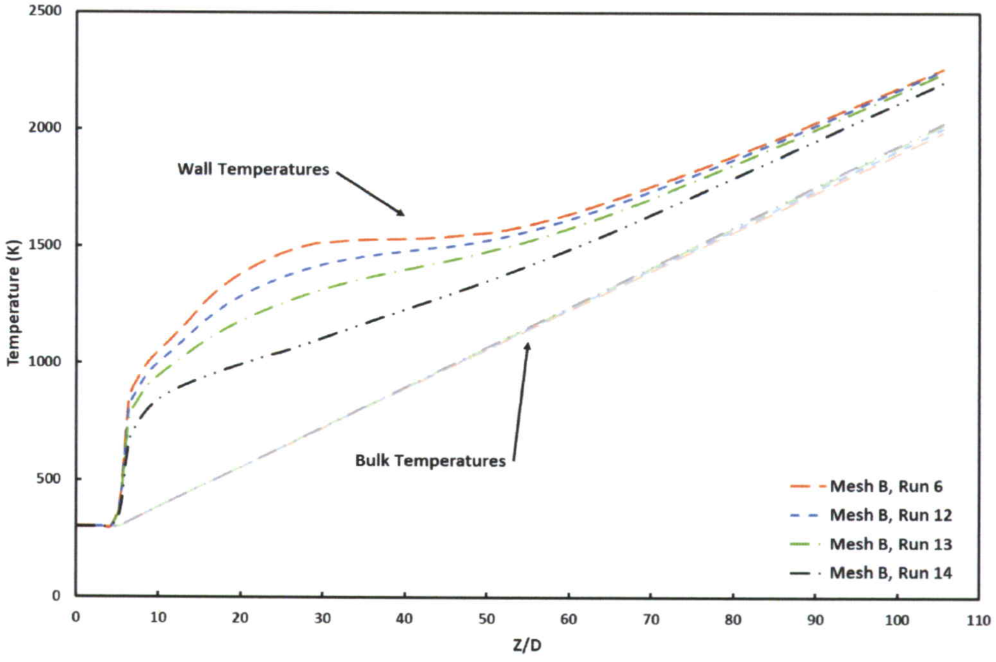

Figure 4.13: Variable Properties, Uniform Flux, Constant Ψ Axial Temperature Profiles

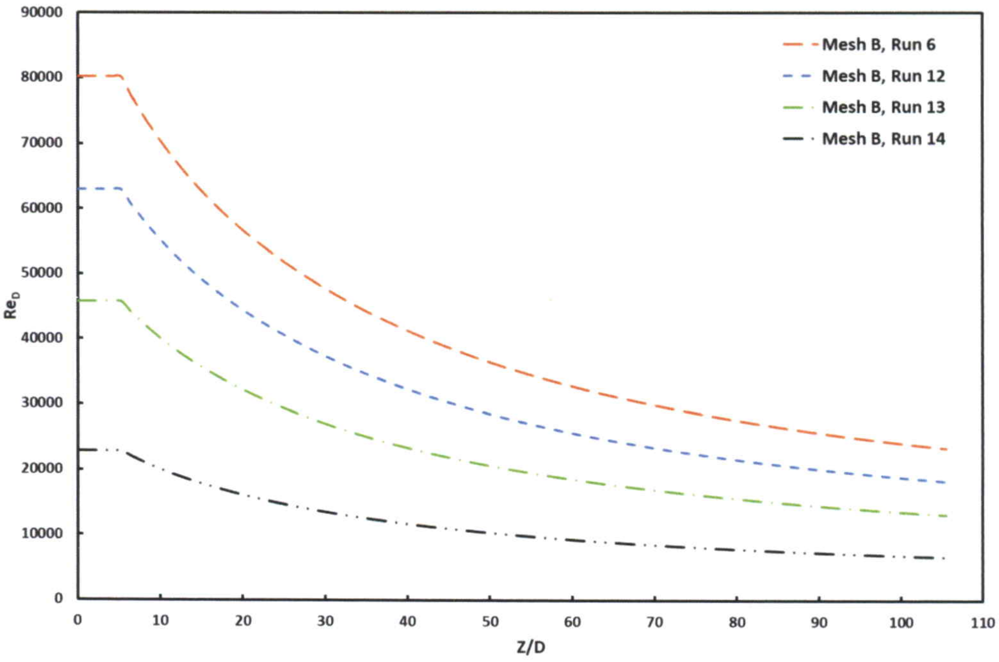

Figure 4.14: Variable Properties, Uniform Flux, Constant Ψ Axial Re$_D$ Profiles

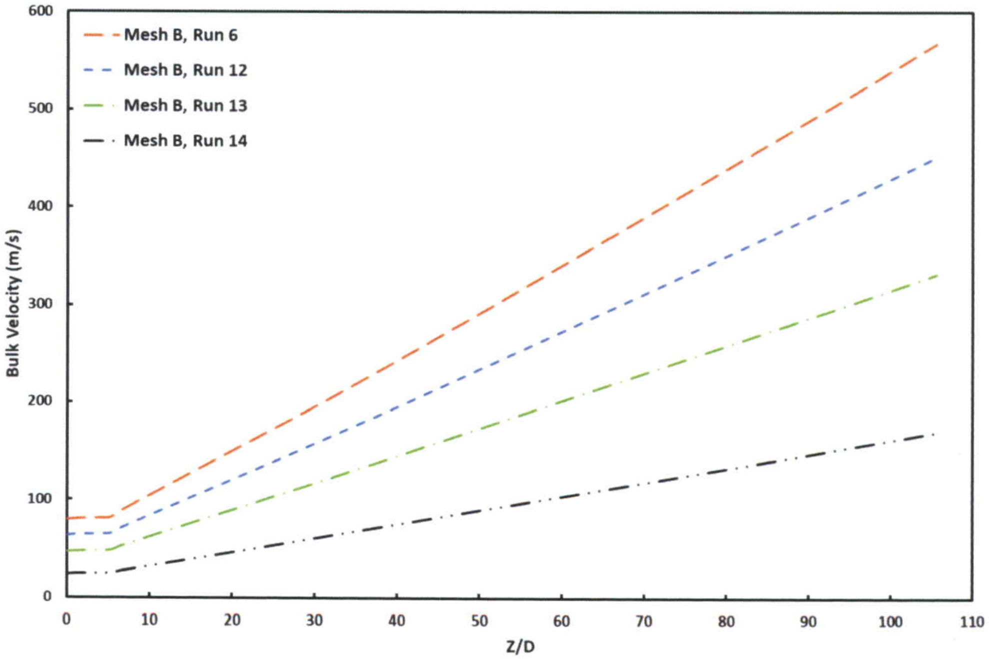

Figure 4.15: Variable Properties, Uniform Flux, Constant Ψ Axial Bulk Velocity Profiles

The bulk temperature rises linearly with the same slope for each case as expected, and the exit wall temperatures trend to a final $T_w \approx 2250\,K$. Run 6 corresponds to NTREES conditions and has been discussed in **Figure 4.8**. The remaining three runs step down the wall heat flux while maintaining the Ψ value and the same out bulk and wall temperatures at the outflow. With decreasing wall heat flux the wall temperature overshoot in axial profiles diminishes. The flow is exposed to less intense wall fluxes and as a result, the radial and axial variation of material properties in the transition region is smaller. This observation lends credence to the idea that the wall temperature overshoot is a physical response in the system enhanced by strongly varying properties as opposed to an artifact in the simulation.

Figure 4.13 was created by holding the outlet temperatures (wall and bulk) fixed while decreasing heat flux. The required the mass flux and therefore the inlet *Re* to decrease as heat flux decreased. A further test of the idea that the non-monotonic axial behavior is due to a heat-flux-driven property change is shown in **Figure 4.16**. Run 6 in orange is common to both **Figures 4.13** and **4.16**. The Nusselt numbers corresponding to **Figure 4.16** are shown in **Figure 4.17**. For these figures, the mass flux, and therefore the inlet *Re* is held constant at values shown in **Table 4.1** for runs 6, 15, 16, and 17. Although the inlet Re_D is constant across these four runs, the two lower flux runs do not show an excess of wall temperature in the developing region. A small excess can be seen in the run with a flux of 2.75 MW/m^2 and the runs with 3.50 MW/m^2 shows a clear excess.

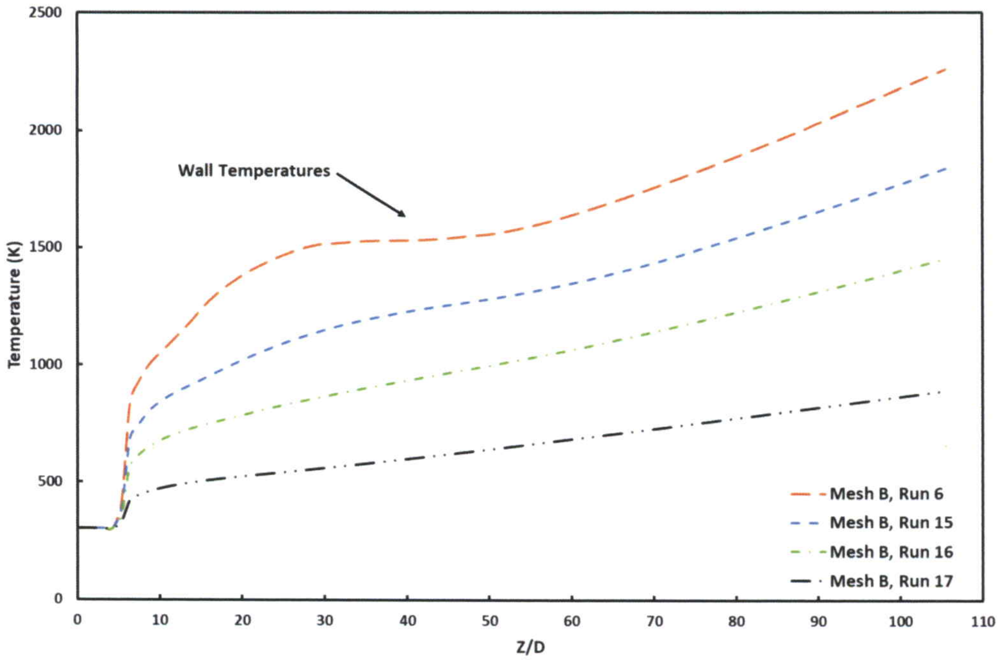

Figure 4.16: Wall Temperature for Variable Properties, Uniform Flux, Constant Mass Flux and Inlet Re_D

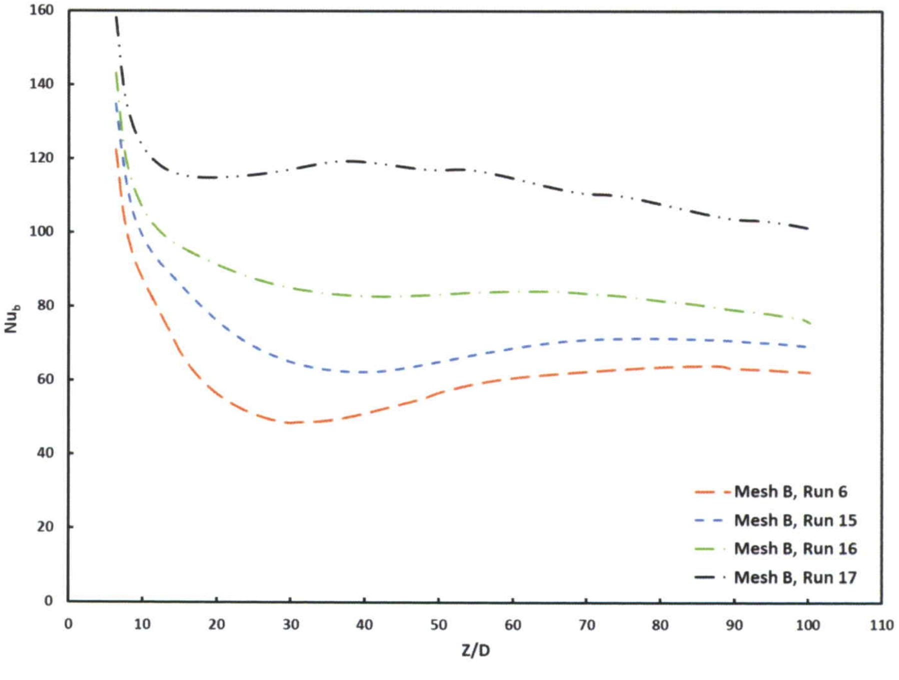

Figure 4.17: Nu_b for Variable Properties, Uniform Flux, Constant Mass Flux and Inlet Re_D

The Nusselt numbers in **Figure 4.17** are differentiated toward the tube outlet because the different levels of heat flux produce different outlet Reynolds numbers. The drop in Nu_b in the development region relative to the outlet value of each run deepens as the heat flux increases. These observations taken together support the idea that property variations in supercritical hydrogen in the state range of interest in NTREES can cause these unexpected excesses of wall temperature in the developing region of the flow under a uniform flux boundary condition.

In a flow such as NTREES, the entire objective of the facility is to further development of NTR fuel rod elements. A known failure mode of these fuel rods dating back to the NERVA program is a mismatch of thermal expansion coefficients between the fissionable fuel material itself and the channel wall cladding which protects the fuel material from being corrosively degraded from exposure to the hot hydrogen gas **[2]**, **[7]**, **[8]**. The mismatch in thermal expansion coefficients is directly related to the coolant channel wall temperature gradients. As the facility is designed to test fuel rod materials to failure in a safe and cost-effective setting, the experimentalists operating the facility need bear inaccurate temperature gradients in mind. **Figure 4.13** is a very powerful demonstrator of how certain flow criteria can over or under embellish other criteria critical in the testing of fuel elements for these unique flow conditions.

Considering the temperature profiles in **Figure 4.13** alone would provoke an engineer to select the boundary conditions of run 14, that is until parameters such as axial Reynolds number (**Figure 4.14**) and velocity (**Figure 4.15**) are reviewed. The flow velocity requirements of NTREES are known to be around $600 - 700\ \frac{m}{s}$ at the exit of the cooling channels **[9]**. It is also an important requirement for the current flow geometry to maintain sufficiently high Reynolds numbers to stay in the turbulent flow regime inside the channels. This is to promote the mixing required for heat transfer within the larger diameter tubes (3.81 mm in diameter) compared to most past work on NTR fuel elements that, historically, had substantially smaller channels. The NERVA program utilized fuel elements comprised of extruded coolant channels 2.36-2.54 mm in diameter **[8]**. Simulations conducted by Cheng (et. al.) **[37]** involved coolant channels 2.04 mm in diameter, while the study done by Appel **[39]** ranged from 1.2-2.4 mm in diameter (see Chapter 2 for further details). Thus, it is required that boundary conditions set for the NTREES facility are similar as those used in run 6. It is shown that run 6 also exhibits the largest temperature gradients and non-monotonic inflection point. Therefore, the boundary conditions selected for flow testing within NTREES must be judiciously selected to best achieve environments found in an actual NTR fuel element without introducing new failure modes that are unique to NTREES alone, a topic that will be discussed in further detail in the following subsection. This concludes the presentation of the variable-properties, uniform flux runs conducted.

Results for Variable Material Properties, Cosine Heat Flux

NTREES Fuel Rod Length

As the NTREES facility is designed to best replicate NTR flow conditions, the current study also investigated the effects a half-cosine wall-heat flux profile had on the coolant channels. See **Equation 3.4** for the cosine power profile used to replicate the nuclear reactor power density distribution typical for a cylindrical volume **[2]**. As with the uniform flux cases, a 5% unheated starting length was added to allow the boundary layer to develop prior to introducing high levels of heat flux to the fluid.

Seen in **Figure 4.18** are the axial temperature profiles produced by the cosine wall heat flux profile applied to a tube length used in the NTREES fuel rod. As in the variable properties, uniform wall-heat flux case investigated, the wall temperature gradient in the streamwise direction was much larger than expected, and there is an inflection present for the developing flow region. The wall inflection may not be as visually obvious in the case of the half-cosine wall-heat flux as it was for uniform heat flux results discussed previously, but what is of more concern is the large difference of wall to bulk temperatures near the inflection. At its maximum, the difference exceeds 1200 K.

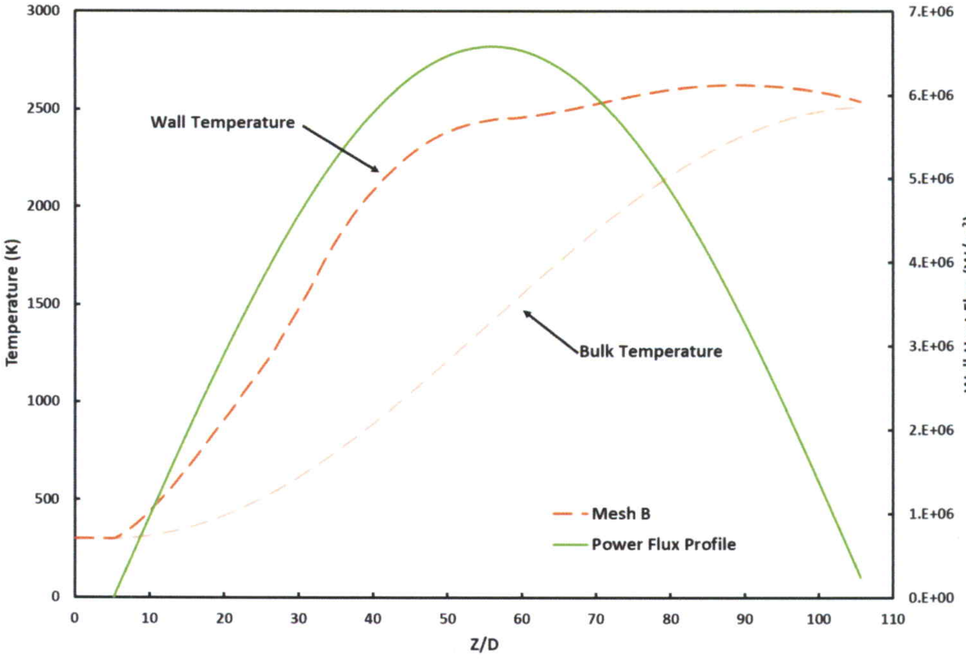

Figure 4.18: Variable Properties, Cosine Flux Axial Temperature and Power Profiles, Tube Length $= 0.4064\ m$

Full NTR Fuel Rod Length

To investigate a typical NTR fuel rod length, the flow geometry was lengthened to 1.2 m. The diameter and radial mesh geometry remained consistent between the two runs. The same half-cosine wall profile (**Equation 3.4**) discussed in Chapter 3 was used. This time mesh C (with a finer axial mesh) was used, as the streamwise geometry was essentially being lengthen by a factor of 3. It was important to increase the streamwise cell divisions from 1500 (mesh B) to 3000 (mesh C) to help maintain axial mesh resolution and reduce large mesh aspect ratios. Recall from Chapter 3 that meshes B and C have identical radial sizing parameters. The mass flux of the 1.2 m geometry simulation was also increased to $\dot{m}'' = 560\ \frac{kg}{m^2 s}$ to create the required equivalent wall exit temperatures and velocity (Review **Table 4-1** for further boundary condition details for run 11).

Seen in **Figure 4.19** are the axial temperature profiles and mathematical cosine wall heat flux profile for the case of a 1.2 m long fuel element. It can be observed that there is little, if any, "bump" or non-monotonic inflection present during the developing stages of the flow. The wall and bulk temperatures differed quite consistently on the order of 280 K. Additionally, once past the peak in the half-cosine wall-heat flux, the rate of enthalpy addition to the flow diminished, as expected, the wall temperature decreased to that of the bulk fluid temperature towards the flow exit. These solution profiles replicated the expected profiles found in previous studies and documentation on NTR flow environments discussed in Chapter 2. This included axial wall temperature plots provided by Emrich **[10]**, Cheng (et. al.) **[37], [38]**, Appel **[39]**, Webb (et. al.) **[40]** and Walton **[42]**. The study conducted by Walton **[42]** produced a thermal-hydraulic analysis code which was validated via NERVA program data itself.

Figure 4.20 compares the power profiles of the two-different geometries (NTREES: $L = 0.4064\ m$ vs. NTR: $L = 1.2\ m$) side by side. If the momentum distributions of both flows are fully developed by $\frac{Z}{D} \approx 60$, the NTR flow is exposed to a much lower heat flux during the developing region. As a result, the wall temperature curve shows no discernable overshoot in temperature.

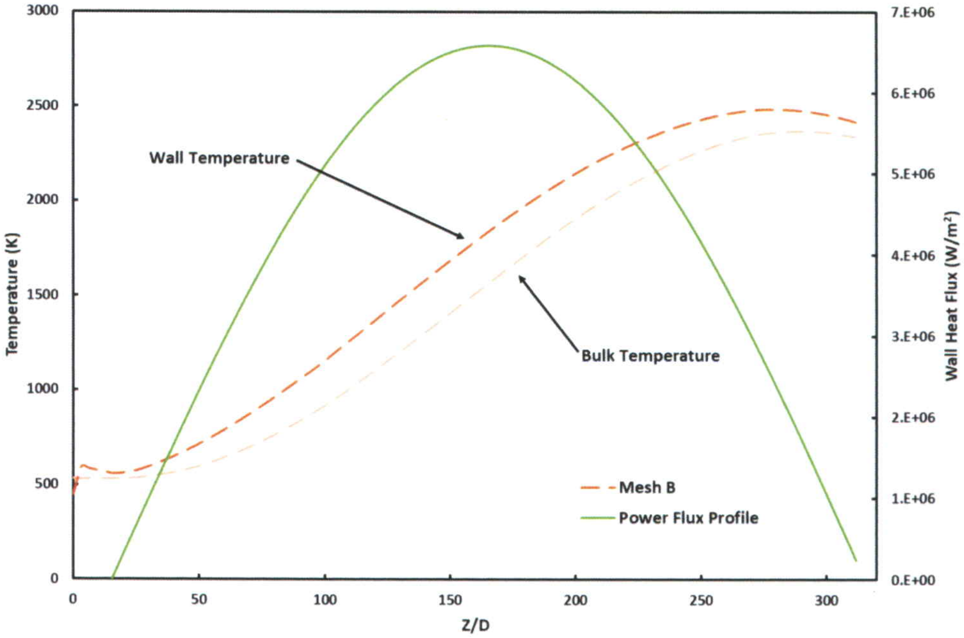

Figure 4.19: Variable Properties, Cosine Flux Axial Temperature and Power Profiles, Tube length $= 1.2\ m$

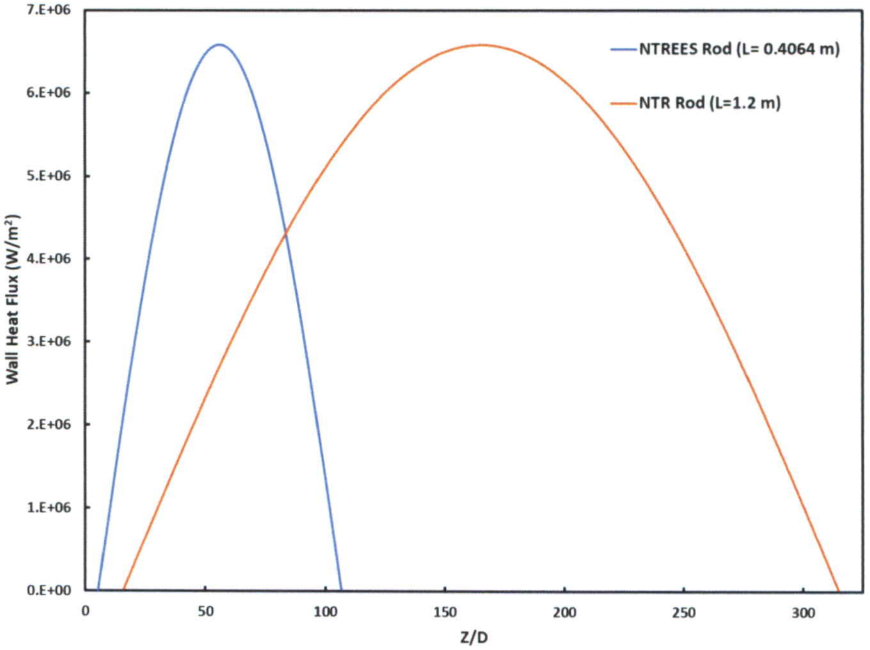

Figure 4.20: Comparison of Cosine Wall-Heat Flux Profiles for a NTREES Fuel Rod Element ($Z = 0.0464\ m$) and a NTR Fuel Rod Element ($Z = 1.2\ m$)

Concluding Remarks

This chapter began with a model validation process using a uniform-property flow with a uniform-heat-flux boundary condition. The solution for this canonical case revealed a small undershoot in skin friction and Nusselt number and a slight overshoot in wall temperature and centerline velocity in the developing region of the tube. These characteristics are not part of typical textbook literature, and there was concern that they could be artifacts of RANS modeling as executed within FLUENT. However, support was found for these observations in the literature reviewed in Chapter 2. Those studies included both experimental work and analytical treatments.

The non-monotonic behavior in the developing region described above was further investigated by introducing the highly variable material properties of supercritical hydrogen – the key feature of this study. Again, a uniform-heat-flux wall boundary condition was selected. It was found that the addition of variable material properties significantly magnified the non-monotonic flow behavior when within the developing flow region. A series (**Figures 4.13 – 4.15**) of variable material properties, uniform-heat-flux simulations were then conducted to determine flow sensitively to hydrogen mass flux and wall-heat flux. The mass flux and heat flux levels were selected to maintain exit wall temperatures, exit bulk velocity and overall bulk fluid temperature. A consequence of this selection is that the inlet Re_D over the tube length increased with increasing heat flux. To examine the effect of heat flux, separate from that of Re_D, another series of runs (**Figures 4.16** and **4.17**) were performed to examine the axial behavior of wall temperature and Nu_b under constant mass flux, constant inlet Re_D, and varying wall heat flux.

With decreasing mass flux and wall-heat flux, the magnitude of the non-monotonic behavior decreased, but was still present. The literature reviewed in Chapter 2 **[22]** also show the magnitude of non-monotonic behavior to increase with higher wall-heat flux and lower mass flux. Our current view is that the primary cause of the non-monotonic behavior in the developing region is due to variable properties for this supercritical fluid and not to the change in Re_D imposed by the constraints of the run shown if **Figure 4.13**. The validation of such a statement will require further research into the role Reynolds number plays on flows of this type. Further discussion of future research can be found in Chapter 6.

As the study foundation was based on NTR fuel rod development and, more specifically, the NTREES facility itself, the case of variable material properties, with a half-cosine wall-heat flux boundary condition was investigated. The results for the 0.4 m tube with NTREES-level heat flux showed a non-monotonic axial wall temperature in the developing flow region. This behavior resulted in both a higher axial temperature gradient and a significantly higher wall temperature over the first one-third to one-half of the tube length. This series of simulation results was then compared against previous research on temperature profiles for NTR fuel elements. Previous studies reviewed showed no presence of a non-monotonic temperature profile in the developing region of the flow. Also, the difference between wall and bulk fluid temperatures were shown to be substantially smaller than that found in runs 8-10 of the current study for a half-cosine wall-heat flux treatment.

To further investigate the discrepancy in this finding compared to past works, the model geometry was lengthened from $L = 0.4064$ m, as found in NTREES, to $L = 1.2$ m for a typical NTR fuel rod length per documents reviewed in Chapter 2. The model results at this tube length yielded comparable axial temperature profiles to past works on NTR flows. The conclusion is that the half-cosine wall flux profile when applied to the longer tube but at the same peak flux level produces a lower wall flux in the developing region. The wall flux levels over the development length for tubes of this length (at the mass flux level selected) are not high enough to create a noticeable non-monotonic behavior in wall temperature. For this reason, past studies may have missed this feature. It should be noted that the results for the uniform-flux cases show little or no effect of heat flux level in the fully developed region on the axial evolution of wall temperature. In the case of the half-cosine wall flux in the 1.2 m NTR tube, the peak flux occurs at $\frac{z}{D} \approx 170$ into the fully developed region where it may leave no imprint on the results.

CHAPTER 5

Study Summary, Future Work and Final Considerations

Study Summary

A computational model of a single cooling channel from an NTREES test element has been produced using a variable-property Reynolds-Averaged Navier-Stokes (RANS) approach. The model was executed in ANSYS-Fluent and required the creation of thermodynamic and thermophysical property tables within Fluent via the User Defined Function (UDF) facility. The single-tube geometry was built within a cartesian coordinate system in such a way that the model can be scaled up to include multiple tubes separated by a solid rod domain. The model was executed for two thermal boundary conditions: uniform wall flux and a cosine-flux axial distribution that is a common model in the NTR community. The results of the study were expected to serve two primary purposes: (1) axial values of heat transfer coefficient (Nusselt number) were produced that can be used in NTREES fuel rod models, and (2) the Nusselt number results can be compared to the predictions of correlations from the literature for flows of this type.

As the work progressed, the following choices and significant efforts were made:

- After a literature survey of works on turbulence transition in internal flows, NTR flows, regenerative cooling flows and other supercritical fluid flows, the k-ω SST turbulence model as implemented in ANSYS-Fluent with standard constants was selected for the study.
- The material properties for supercritical hydrogen at the temperatures and pressures required in this study were introduced into ANSYS-Fluent via custom coding through Fluent's UDF facility. This effort was a significant enabling accomplishment in performing these simulations.
- A domain resolution study yielded the element mesh labeled "mesh B" with 1,246,500 elements as acceptable for the study. All meshes considered monotonically converged to a single solution profile without run-time instability.
- A total of 17 simulation runs were conducted and analyzed for a single tube at turbulent Reynolds numbers with uniform wall heat flux or a half-cosine distribution of wall heat flux modeled via ANSYS-Fluent UDF code facility.
- A study of the literature regarding heat transfer into supercritical hydrogen revealed a substantial number of Nusselt number correlations which were applicable to the current study.

The primary observations were:

- ANSYS-Fluent with both the *k-ω* SST and *k-ε* turbulence models yielded undershoots in Nusselt number and skin friction coefficient and an overshoot in wall temperature and centerline velocity in the developing region of the flow. This non-monotonic axial behavior was just visible even in constant-property runs. These characteristics are not part of typical textbook literature, and there was concern that they could be artifacts of RANS modeling as executed within ANSYS-Fluent. However, support was found for these observations in the literature from both experimental work and analytical treatments.

- The non-monotonic behavior in the developing region became clearly evident when the highly variable material properties of supercritical hydrogen were introduced. This outcome was most specifically evident for the 0. 4 m tube with NTREES-level heat flux. Our current view is that the primary cause of the non-monotonic behavior in the developing region is due to variable properties for this supercritical fluid with the axial change in Reynolds number imposed by axial property change appearing as a complicating factor.

- Previous studies of NTR geometries showed no presence of a non-monotonic temperature profile in the developing region of the flow. However, the difference between wall and bulk fluid temperatures in these studies was substantially smaller than in the present study. To investigate the discrepancy in this finding compared to past works, the tube length was increased to 1.2 m for a typical NTR fuel rod found in past studies. The model results at this tube length yielded comparable axial temperature profiles to past works on NTR flows. The conclusion is that the half-cosine wall flux profile when applied to the longer tube but at the same peak flux level produces a lower wall flux in the developing region. The wall flux levels over the development length for tubes of this length (at the mass flux level selected) are not high enough to create a noticeable non-monotonic behavior in wall temperature. For this reason, past studies may have missed this feature.

- None of the heat transfer correlations reviewed in past studies captured the behavior of the Nusselt number in the developing region of the simulations with high wall-heat flux levels.

Future Work and Final Considerations

- The current study can be looked at as a preliminary foundation stage of model development for a suite of models catered to the unique needs of the NTREES facility. Model coordinate systems and UDF coding was set up in such a way that a scale up could quickly be implemented. These scale ups could include multiple coolant channels, modeling the NTREES chamber convective/radiative energy losses and different propellant gases other than hydrogen being implemented. Also, NTREES is known to have more of a "Top-Hat" wall-heat flux profile due to the inductive heating coil. Thus, the propellant cooling channel wall-heating profiles will reside somewhere in between a uniform wall-heat flux and a half-cosine flux profile as the heat will disperse into the solid fuel element prior to being advected away by the hydrogen propellant. To model such a profile, a solid tungsten rod conjugate heat transfer model addition would be required.

- Future work into the development of a Nusselt number correlation is needed. None of the heat transfer correlations reviewed in past studies captured the behavior of the Nusselt number in the developing region of the simulations with high wall-heat flux levels. The most accurate and most widely accepted supercritical hydrogen flow correlation reviewed being developed by Taylor **[19]**.

- Further investigation into the phenomena causing non-monotonic inflection in both radial and axial flow parameter profiles is required. The phenomena are present in both momentum and thermal profiles. The present results and examples from the literature show the occurrence of non-monotonic profiles to increase with higher wall-heat flux and lower mass flux. Also, when the Reynolds number decreased and approached the transitioning regime back to laminar flow. The research group believes these results can be split into separate groupings. The flow investigated in the current study showed the non-monotonic behavior to subside with decreasing Reynolds number. This is against the findings reviewed on similar flows discussed in Chapter 2. However, it is thought that this effect is masked by the severity wall-heat flux plays on the flow. The validation of such a statement will require further research into the role Reynolds number itself specifically plays on flows of this type.

REFERENCES

[1] Brown, Charles D., *Elements of Spacecraft Design*. American Institute of Aeronautics and Astronautics, 2002.

[2] Emrich, William Jr., *Principles of Nuclear Rocket Propulsion*. Elsevier, Butterworth-Heinemann, 2016.

[3] Khatry, Jivan; Aydogan, Fatih; Ilyas, Muhammad; Houts, Michael, "Design of a passive safety system for a nuclear thermal rocket", *Annals of Nuclear Energy*, vol. 111, pp. 536-553, 2017.

[4] Howe, Steven D., "Assessment of the Advantages and Feasibility of a Nuclear Rocket for a Manned Mars Mission, LA-UR-85-2442", *Los Alamos National Laboratory*, Los Alamos, NM, June 10-14 1985.

[5] Borowski, Stanley K.; McCurdy, David R.; Packard, Thomas W., "'7-Launch' NTR Space Transportation Option for NASAs Mars Design Reference Architecture (DRA) 5.0", *45th AIAA/ASME/SAE/ASEE Joint Propulsion Conference &Amp; Exhibit*, February 2009.

[6] Borowski, Stanley K., "Nuclear Thermal Propulsion: Past Accomplishments, Present Efforts, and a Look Ahead", *Journal of Aerospace Engineering*, vol. 26, no. 2, 2013, pp. 334–342.

[7] Fittje, James; Bruce, Schnitzler, "Evaluation of Recent Upgrades to the NESS (Nuclear Engine System Simulation) Code." *44th AIAA/ASME/SAE/ASEE Joint Propulsion Conference &Amp; Exhibit*, 2008.

[8] Taub, J. M., "A Review of Fuel Element Development for Nuclear Rocket Engines, LA-5931", *Los Alamos National Laboratory*, Los Alamos, NM, p. 18, June 1975.

[9] Emrich, William Jr., *Personal Email Correspondence*, June 2017.

[10] Emrich, William Jr., "Nuclear Thermal Rocket Element Environmental Simulator (NTREES)". *PowerPoint presentation*. June 2017.

[11] Dewar, James A., *To the End of the Solar System: The Story of The Nuclear Rocket*, 2nd edn. Apogee Books, 2007.

[12] Robbins, W.H.; Finger, H.B., "An Historical Perspective of the NERVA Nuclear Rocket Engine Technology Program, NASA Contractor Report 187154, NASA Contract NAS3-25266, AIAA-91-3451," *Lewis Research Center*, Cleveland, OH, July 1991.

[13] Koenig, Daniel R., "Experience Gained from the Space Nuclear Rocket Program (Rover), LA-10062-H", *Los Alamos National Laboratory*, Los Alamos, NM, May 1986.

[14] McAdams, W. H., *Heat Transmission*, 2nd edn., McGraw-Hill, New York, NY, 1942.

[15] Mills, A.F.; Coimbra, C.F.M., *Heat Transfer*, 3rd edn., Temporal Publishing, San Diego, CA, 2016.

[16] Genic, S.; Arandjelovic, I.; Kolendic, P.; Jaric, M.; Budimir, N.; Genic, V., "A Review of Explicit Approximations of Colebrook's Equation", *Faculty of Mechanical Engineering Transactions, Belgrade*, Serbia, Vol. 39, pp 67-71, 2011.

[17] Welty, J. R.; Rorrer, G.L.; D.G. Foster, D.G., *Fundamentals of Momentum, Heat, and Mass Transfer*, 6th edn., Wiley, NJ, 2014.

[18] Thomas, G.R., "An Interim Study of Single-Phase Heat Transfer Correlations Using Hydrogen, WANL-TNR-056", *Westinghouse Electric Corporation Astronuclear Laboratory*, PA, April 1962.

[19] Taylor, Maynard F., "Correlation of Local Heat-Transfer Coefficients for Single-Phase Turbulent Flow of Hydrogen in Tubes with Temperature Ratios to 23, NASA TN D-4332", *NASA*, Washington D.C., January 1968.

[20] Taylor, Maynard F., "Experimental Local Heat-Transfer and Average Friction Data for Hydrogen and Helium Flowing in a Tube at Surface Temperatures up to 5600° R, NASA TN D-2280", *NASA*, Washington D.C., April 1964.

[21] Taylor, Maynard F., "Prediction of Friction and Heat-Transfer Coefficients with Large Variation in Fluid Properties, NASA TM X-2145", *NASA*, Washington D.C., December 1970.

[22] Youn, B.; Mills, A.F., "Flow of Supercritical Hydrogen in a Uniformly Heated Circular Tube", *Department of Mechanical, Aerospace and Nuclear Engineering, University of California*, Los Angeles, CA, 1993.

[23] Taylor, Maynard F., "A Method of Predicting Heat Transfer Coefficients in the Cooling Passages of NERVA and PHOEBUS-2 Rocket Nozzles, NASA TM X-52437", *NASA*, Washington D.C., 1968.

[24] Slaby, Jack G.; Mattson, William F., "Heat-Transfer Coefficients for Hydrogen Flowing Through Parallel Hexagonal Passages at Surface Temperatures to 2275K, NASA TN D-4959", *NASA*, Washington D.C., December 1968.

[25] Donne, Dalle M.; Tartaglia, G.P., "Heat Transfer for Turbulent Flow of Helium or Hydrogen in a Tube at Hight Temperatures: Evaluation with the Method of Petukhov, KFK 3593, EUR 7988e", *Karlsruher Institute for Nuclear Physics and Reactor Physics Technology*, Eggenstein-Leopoldshafen, Germany, September 1983.

[26] McEligot, D.M.; Magee, D.M.; Leppert, G., "Effect of Large Temperature Gradients on Convective Heat Transfer: The Downstream Region", *Journal of Heat Transfer* Vol. 87, Series C, No. 1, 67, 1965.

[27] Pfriem, H.J., "Turbulent Heat Transfer to Helium and Hydrogen in Heated Tubes with Large Axially Increasing Temperature Differences" *Proc. Int. Meet Reactor Heat Transfer*, edn. M, Dalle Donne, Kernforschungszentrum Karlsrushe, p. 301, October 9-11 1973.

[28] Chen, Y.T.; Nie, J.H.; Armaly, B.F.; Hsieh, H.T.; Boehm, R.F., "Developing Turbulent Forced Convection in Two-Dimensional Duct", *Journal of Heat Transfer*, Vol. 129, pp. 1295-1299, September 2007.

[29] Deissler, Robert G., "Analysis of Turbulent Heat Transfer and Flow in the Entrance Regions of Smooth Passenges, NACA TN-3016", *Lewis Flight Propulsion Laboratory*, Cleveland, OH, October 1953.

[30] Deissler, Rober G., "Analysis of Turbulent Heat Transfer, Mass Transfer, and Friction in Smooth Tubes at High Prandtl and Schmidt Numbers, NACA TN-3145, *Lewis Flight Propulsion Laboratory*, Cleveland, OH, May 1954.

[31] Duz, H., "Numerical Flow Analysis of The Variation of Central Axial Velocity Along the Pipe Inlet" *The Eurasia Proceedings of Science, Technology, Engineering & Mathematics (EPSTEM)*, Vol. 2, pp. 323-333, 2018.

[32] Doherty, J.; Ngan, P.; Monty, J.; Chong, M.; "The Development of Turbulent Flow", *Department of Mechanical Engineering, The University of Melbourne*, Parkville, Australia, December 2007.

[33] Malik, Mujeeb Rehman, "Prediction of Laminar and Turbulent Flow Heat Transfer in Annual Passages", *Iowa State University*, Dissertation, 1978.

[34] McCarty, R.D.; Hord, J.; Roder, H. M., *Selected Properties of Hydrogen (Engineering Design Data)*, NBS Monograph 168, National Bureau of Standards, Boulder, CO, 1981.

[35] Dang, G.; Zhong, F.; Zhang, Y.; Zhang, X.; "Numerical Study of Heat Transfer Deterioration of Turbulent Supercritical Kerosene Flow in Heated Circular Tube", *International Journal of Heat and Mass Transfer*, Vol. 85, pp. 1003-1011, March 2015.

[36] Locke, J.M.; Landrum, D.B.; "Uncertainty Analysis of Heat Transfer to Supercritical Hydrogen in Cooling Channels, AIAA-2005-4303", *Propulsion Research Center, University of Alabama in Huntsville*, Huntsville, AL, 2005.

[37] Cheng, Gary; Ito, Yasushi; Ross, Doug; Chen, Yen-Sen; Wang, Ten-See, "Numerical Simulations of Single Flow Element in a Nuclear Thermal Thrust Chamber, NASA MSFC-240", *NASA MSFC*, Huntsville, AL, 2007.

[38] Cheng, Gary; Wang, Ten-See; Canabal, Francisco; Chen, Yen-Sen; Ito, Yasushi, "Thermal Hydraulics Design and Analysis Methodology for a Solid-Core Nuclear Thermal Rocket Engine Thrust Chamber", *NASA MSFC*, Huntsville, AL, January 2013.

[39] Appel, Brad, "Multiphysics Design and Simulation of a Tungsten-Cermet Nuclear Thermal Rocket", *The University of Texas A&M*, Thesis, August 2012.

[40] Webb, Jonathan A.; Gross, Brian; Taitano, William T., "A Combined Neutronic-Thermal Hydraulic Model of a Cermet NTR Reactor, Nuclear and Emerging Technologies for Space 2011 Paper 3276", *Proceedings of Nuclear and Emerging Technologies for Space*, Albuquerque, NM, February 2011.

[41] Peery, Steven D.; Parsley, Randy C.; Anghaie, Samim; Feller, Gerald J., "XNR2000 – A Near Term Nuclear Thermal Rocket Concept, AIP-CONF-930103", *American Institute of Physics*, 1993.

[42] Walton, James T., "Program ELM: A Tool for Rapid Thermal-Hydraulic Analysis of Solid-Core Nuclear Rocket Fuel Elements, NASA-TM-105867", *NASA*, Cleveland, OH, November 1992.

[43] Chase, M.W. Jr.; *NIST-JANAF Thermochemical Tables*, 4th edn., J. Phys. Chem. Ref. Data, Monograph 9, pp. 1-1951, 1998.

[44] *"Manual Set Information"*, *ANSYS Fluent 16.0 User Theory Guide*, 29 June 2015.

[45] Notter, R.H.; Sleicher, C.A.; "A Solution to the Turbulent Graetz Problem-III Fully Developed and Entry Region Heat Transfer Rates", *Chemical Engineering Science*, Vol. 27, pp. 2073-2093, March 1972.

[46] "ANSYS Fluent UDF Manual", *ANSYS Fluent 15.0 UDF Manual*, November 2013.

[47] McCarty, R.D.; "Hydrogen Technological Survey – Thermophysical Properties, NASA SP-3089", *Cryogenics Division, Institute for Basic Standards, National Bureau of Standards*, Boulder, CO, 1975.

[48] Menter, F. R., "Zonal Two Equation k-ω Turbulence Models for Aerodynamic Flows", AIAA Paper 93-2906, 1993.

[49] Kays, W.; Crawford, M.; Weigand, B., “Convective Heat and Mass Transfer”, *McGraw-Hill* 3th edn., McGraw-Hill, New York, NY, 1993.

[50] Pope, Stephen B., “Turbulent Flows”, *Cambridge University Press*, 2000.